The O_2 A-Band in the Fluxes and Polarization of Starlight Reflected by Earth-Like Exoplanets

Fauchez, Thomas; Rossi, Loic; Stam, Daphne M.

DOI
10.3847/1538-4357/aa6e53

Publication date
2017

Document Version
Final published version

Published in
The Astrophysical Journal: an international review of astronomy and astronomical physics

The Astrophysical Journal, 842:41 (18pp), 2017 June 10 https://doi.org/10.3847/1538-4357/aa6e53

The O_2 A-Band in the Fluxes and Polarization of Starlight Reflected by Earth-Like Exoplanets

Thomas Fauchez[1], Loic Rossi[2], and Daphne M. Stam[2]
[1] Laboratoire d'Optique Atmosphèrique (LOA), UMR 8518, Université Lille 1, Villeneuve d'Ascq, France
[2] Faculty of Aerospace Engineering, Delft University of Technology, Kluyverweg 1, 2629 HS Delft, The Netherlands
Received 2016 December 15; revised 2017 March 14; accepted 2017 April 18; published 2017 June 12

Abstract

Earth-like, potentially habitable exoplanets are prime targets in the search for extraterrestrial life. Information about their atmospheres and surfaces can be derived by analyzing the light of the parent star reflected by the planet. We investigate the influence of the surface albedo A_s, the optical thickness b_{cloud}, the altitude of water clouds, and the mixing ratio of biosignature O_2 on the strength of the O_2 A-band (around 760 nm) in the flux and polarization spectra of starlight reflected by Earth-like exoplanets. Our computations for horizontally homogeneous planets show that small mixing ratios ($\eta < 0.4$) will yield moderately deep bands in flux and moderate-to-small band strengths in polarization, and that clouds will usually decrease the band depth in flux and the band strength in polarization. However, cloud influence will be strongly dependent on properties such as optical thickness, top altitude, particle phase, coverage fraction, and horizontal distribution. Depending on the surface albedo and cloud properties, different O_2 mixing ratios η can give similar absorption-band depths in flux and band strengths in polarization, especially if the clouds have moderate-to-high optical thicknesses. Measuring both the flux and the polarization is essential to reduce the degeneracies, although it will not solve them, especially not for horizontally inhomogeneous planets. Observations at a wide range of phase angles and with a high temporal resolution could help to derive cloud properties and, once those are known, the mixing ratio of O_2 or any other absorbing gas.

Key words: planetary systems – polarization – techniques: polarimetric

1. Introduction

After more than two decades of exoplanet detections, statistics show that, on average, every star in the Milky Way has a planet, and at least 20% of the solar-type stars have a rocky planet in their habitable zones (Petigura et al. 2013). The habitable zone is the region around a star where a planet receives the right amount of energy to allow water to be liquid on its surface (see, e.g., Kasting et al. 1993) (assuming they have a solid surface).[3] Recently, Proxima Centauri, the star closest to our Sun, was shown to host a potentially rocky planet in its habitable zone (Anglada-Escudé et al. 2016). Planets in habitable zones are prime targets in the search for extraterrestrial life, because liquid water is essential for life as we know it. Whether or not a rocky planet has liquid surface water also depends on the thickness, composition, and structure of its atmosphere. Narrowing down planets in our search for extraterrestrial life thus requires the characterization of planetary atmospheres in terms of composition and structure, as well as surface pressure and albedo. Of particular interest is the search for biosignatures—i.e., traces of present or past life, such as the atmospheric gases oxygen and methane—and for habitability markers, such as liquid surface water.

Gases such as oxygen and methane are too chemically reactive to remain in significant amounts in any planetary atmosphere without continuous replenishment. The current globally averaged mixing ratio of biosignature (and greenhouse gas) methane is much smaller than that of dioxygen, i.e., only about $1.7 \cdot 10^{-6}$. Also due to its distinct sources, its distribution varies both horizontally and vertically across the Earth and in time. The dioxygen mixing ratio in the current Earth's atmosphere is about 0.21 and virtually altitude-independent. Although oxygenic photosynthetic organisms appeared about $3.5 \cdot 10^9$ yr ago, the oxygen they produced was efficiently chemically removed from the atmosphere by combining with dissolved iron in the oceans to form banded iron formations (Crowe et al. 2013). It is thought that when this oxygen sink became saturated, the atmospheric free oxygen started to increase in the so-called Great Oxygenation Event (GOE) around $2.3 \cdot 10^9$ yr ago. While after the GOE, the oxygen mixing ratio remained fairly low and constant at about 0.03 for about 10^9 yr, at that point it started to rise rapidly to maximum levels of 0.35 about $2.80 \cdot 10^8$ yr ago. Since then, the ratio has leveled off to its current value (Crowe et al. 2013). The triatomic form of oxygen, ozone, is formed by photodissociation of dioxygen molecules. Ozone protects the Earth's biosphere from harmful UV radiation by absorbing it. The ozone mixing ratio is variable and shows a prominent peak between about 20 and 30 km of altitude, the so-called ozone layer.

In this paper, we investigate the planetary properties that determine the appearance of gaseous absorption bands in the spectra of starlight reflected by exoplanets with Earth-like atmospheres. We concentrate on the so-called O_2 A-band, centered around 760 nm, the strongest absorption band of O_2 across the visible. The advantage of concentrating on this band is not only that it appears to be a strong biosignature but also that the range of absorption optical thicknesses across the band is large and thus probes virtually all altitudes within an atmosphere (assuming it is well-mixed throughout the atmosphere). The identification of biosignatures such as oxygen and methane in an exoplanet signal will depend on the presence of the spectral features they leave in a planetary spectrum. The retrieval of the mixing ratio of an atmospheric gas will rely on the strength of the spectral features. This strength with respect to the continuum surrounding a feature will depend on the

[3] Moons that orbit planets in a habitable zone could also be habitable.

intrinsic strength of the feature, i.e., the absorption cross-section of the molecules and their atmospheric column number density (in molecules m^{-2}). It will also be affected by clouds in the atmosphere, as they will cover (part) of the absorbing molecules and change the optical path lengths of the incoming photons, thus changing the amount of absorption (Fujii et al. 2013). The precise influence of the clouds will depend on the (horizontal and vertical) distribution of the absorbing gases and on the cloud properties: their horizontal and vertical extent, cloud particle column number densities, and cloud particle microphysical properties, such as particle size distribution, composition, and even shape. Through the cloud particle microphysical properties, the influence of clouds on the spectral features of atmospheric gases will thus also depend on the wavelength region under consideration.

On Earth, the O_2 mixing ratio is known and constant up to high altitudes. Therefore, as postulated by Yamamoto & Wark (1961) and demonstrated by Fischer & Grassl (1991) and Fischer et al. (1991), the depth of the O_2 A-band in the spectra of sunlight reflected by a region of the Earth that is covered by an optically thick cloud layer allows an estimate of cloud-top altitudes. Because of the strength of the O_2 A-band, this method is sensitive to both high and low clouds and appears to be insensitive to temperature inversions. The method is widely applied both to measurements taken from airplanes (e.g., Lindstrot et al. 2006) and to satellite data (see Saiedy et al. 1965; Vanbauce et al. 1998; Koelemeijer et al. 2001; Preusker et al. 2007; Lelli et al. 2012; Desmons et al. 2013). However, because this method only accounts approximately for the penetration and multiple scattering of photons inside the cloud, it tends to systematically overestimate cloud-top pressures (hence, it underestimates cloud-top altitudes; Vanbauce et al. 1998). The retrieved pressure appears to be more representative of the pressure halfway through the cloud (see Vanbauce et al. 2003; Sneep et al. 2008; Wang et al. 2008; Ferlay et al. 2010; Desmons et al. 2013).

In Earth remote sensing, the retrieval of cloud-top altitudes is important for climate research, especially for the retrieval of atmospheric column densities of trace gases, such as ozone and methane, that will be partly hidden from the view of Earth-orbiting satellites when clouds are present. Not surprisingly, there is little interest in deriving O_2 mixing ratios.

In exoplanet research, however, the O_2 mixing ratio is unknown, and absorption-band depths cannot be used to derive cloud-top altitudes. Indeed, the direct detection of exoplanetary radiation in order to investigate the depth of gaseous absorption bands is extremely challenging because of the huge flux contrast between a parent star and an exoplanet and the small angular separation between the two. Konopacky et al. (2013) were the first to succeed in capturing a thermal spectrum of one of the exoplanets around the star HR 8799 by spatially separating it from its star. The spectrum of this young and hot, and thus thermally bright, planet shows molecular lines from water and carbon monoxide. Because of their moderate temperatures, potentially habitable exoplanets will not be very luminous at infrared wavelengths, and the relatively small size of rocky exoplanets will require highly optimized telescopes and instruments for their characterization. Examples of current instruments that aim to spatially resolve large, gaseous, old, and cold exoplanets from their parent stars and characterize them from their directly detected signals are the Spectro-Polarimetric High-contrast Exoplanet Research (SPHERE; see Beuzit et al. 2006 and references therein) on the European Southern Observatory's Very Large Telescope (VLT), the Gemini Planet Finder (GPI; see Macintosh et al. 2014) on the Gemini North telescope, the Coronographic High Angular Resolution Imaging Spectrograph (CHARIS; see Groff et al. 2014) on the Subaru telescope, and the High-Resolution Optical Spectrograph (HROS) on the future Thirty Meter Telescope (TMT; Froning et al. 2006; Osterman et al. 2006). The future European Extremely Large Telescope (E-ELT) also has the characterization of Earth-like exoplanets as one of its main science cases.

Both SPHERE and GPI can measure not only the thermal fluxes that their target planets emit and the fluxes of starlight that the planets reflect, they can also measure the state of polarization of the planetary radiation. In particular, SPHERE has a polarimetric optical arm that is based on the Zürich Imaging Polarimeter (ZIMPOL) technique (Gisler et al. 2004; Schmid et al. 2005). IRDIS, an infrared arm of SPHERE, has polarimetric capabilities that are designed for observations of circumstellar matter but potentially of use for exoplanet detection, too. Polarimetry is also a technique that will be used in the Earth-like Planet Imaging Camera System (EPICS; Keller et al. 2010; Gratton et al. 2011) that is being planned for the E-ELT. First detections of polarimetric signals of exoplanets have been claimed (see Wiktorowicz et al. 2015; Bott et al. 2016 and references therein).

There are several advantages of using polarimetry in exoplanet research. First, the light of a solar-type star can be assumed to be unpolarized (see Kemp et al. 1987) when integrated across the stellar disk, while starlight that has been reflected by a planet will usually be (linearly) polarized (see, e.g., Seager et al. 2000; Stam et al. 2004; Stam 2008). Polarimetry can thus increase the much-needed contrast between a planet and its parent star (Keller 2006) and facilitate the direct detection of an exoplanet. Second, detecting a polarized object in the vicinity of a star would immediately confirm the planetary nature of the object, as stars or other background objects will have a negligible-to-low degree of polarization. Third, the state of polarization of the starlight (particularly as a function of the planetary phase angle and/or wavelength) that has been reflected by the planet is sensitive to the structure and composition of the planetary atmosphere and surface and could thus be used for characterizing the planet, e.g., by detecting clouds and hazes and their composition. A famous example of this application of polarimetry is the derivation of the size and composition of the cloud droplets that form the ubiquitous Venus clouds from disk-integrated polarimetry of reflected sunlight at three wavelengths and across a broad phase angle range by Hansen & Hovenier (1974) (thus, observations similar to those that would be available for direct exoplanet observations, with the exoplanet's phase angle range depending on the orbital inclination angle). These cloud particle properties, which were later confirmed by in situ measurements, could not be derived from the spectral and phase angle dependence of the sunlight's reflected flux, because flux phase functions are generally less sensitive to the microphysical properties of the scattering particles. For exoplanets, Karalidi et al. (2012) and Bailey (2007) have numerically shown that the primary rainbow of starlight that has been scattered by liquid water cloud particles on a planet should be observable for relatively small water cloud coverage (CC; 10%–20%), even when the liquid water clouds are partly

covered by ice water clouds (which themselves do not show the rainbow feature). In Earth observation, the PARASOL/POLDER instrument series (Deschamps et al. 1994; Fougnie et al. 2007) uses polarimetry to determine the phase of the (water) clouds it observes (see, e.g., Goloub et al. 2000).

In this paper, we investigate the influences on the O_2 A-band in not only the flux spectra of starlight that is reflected by exoplanets but also in the polarization spectra. Indeed, gaseous absorption bands not only show up in the flux spectra of light reflected by (exo)planets, they usually also appear in the polarization spectra (see Stam et al. 1999; Aben et al. 2001; Stam et al. 2004; Joos & Schmid 2007; Boesche et al. 2008, for examples in the solar system).

There are two main reasons why absorption bands appear in polarization spectra despite polarization being a relative measure, i.e., the polarized flux divided by the total flux. First, with increasing absorption, the reflected light contains less multiple scattered light, which usually has a lower polarization than singly scattered light. The relative increase of the contribution of singly scattered light to the reflected signal thus increases its degree of polarization. Second, with increasing absorption, the altitude at which most of the reflected light has been scattered increases. If different altitude regions of the atmosphere contain different types of particles with different single-scattering polarization signatures, the polarization will vary across an absorption line, with the degree of polarization in the deepest part of the line representative of the particles in the higher atmospheric layers and that in the continuum representative of the particles in the lower, usually denser atmospheric layers. For an in-depth explanation of these effects, see Stam et al. (1999). Note that, while attenuation through the Earth's atmosphere will change the flux of an exoplanet, it does not change the degree of polarization across the gaseous absorption bands in a spectrum of a planet or exoplanet. This is an additional advantage of using polarimetry for the detection of gaseous absorption bands with ground-based telescopes, in particular when (exo)planet observations are pursued in wavelength regions where the Earth's atmosphere itself absorbs light.

The results presented in this paper are not just useful in investigating the retrieval of trace gases and cloud properties of exoplanets. They will also be useful for the design and optimization of spectrometers for exoplanetary detection and characterization. The optical response of mirrors, lenses, and gratings usually depends on the degree and direction of the light that is incident on them; when observing a polarized signal, such as starlight that has been reflected by an exoplanet, the detected flux signal will depend on the degree and direction of polarization of the incoming light. In particular, the detected depth of a gaseous absorption band, and hence the gaseous mixing ratio that will be derived from it, depends on the polarization across the band. Even if a telescope's and/or instrument's polarization sensitivities are fully known, detected fluxes can only be accurately corrected for polarization sensitivities if the polarization of the observed light is measured as well (see Stam et al. 2000a for examples of such corrections). In the absence of such polarization measurements, numerical simulations such as those presented in this paper can help to assess the uncertainties.

The structure of this paper is as follows. In Section 2, we describe our method for calculating the flux and polarization of starlight that is reflected by an exoplanet, including our disk-integration technique and how we handle the spectral computations. In Section 3, we present our numerical results for cloud-free, completely cloudy, and partly cloudy exoplanets. Finally, in Sections 4 and 5, we discuss and summarize our results.

2. Calculating Reflected Starlight

2.1. Flux Vectors and Polarization

The flux and state of polarization of starlight that is reflected by a spatially unresolved exoplanet and received by a distant observer is fully described by a flux (column) vector,

$$\pi \boldsymbol{F} = \pi [F, Q, U, V], \tag{1}$$

where πF is the total flux, πQ and πU are the linearly polarized fluxes defined with respect to a reference plane, and πV is the circularly polarized flux (for details on these parameters, see, e.g., Hansen & Travis 1974; Hovenier et al. 2004). We use the planetary scattering plane—i.e., the plane through the centers of the planet, star, and observer—as the reference plane for parameters Q and U.

Integrated over the stellar disk, the light of a solar-type star can be assumed to be virtually unpolarized (Kemp et al. 1987). We thus describe its flux vector as $\boldsymbol{\pi F}_0 = \pi F_0 [1, 0, 0, 0] = \pi F_0 \mathbf{1}$, where πF_0 is the stellar flux measured perpendicular to the direction of propagation of the light and $\mathbf{1}$ is the unit (column) vector.

Integrated over the illuminated and visible part of a planetary disk, the starlight that is reflected by a planet will usually be linearly polarized, with the degree of polarization depending on the properties of the planetary atmosphere and surface (if present; see, e.g., Stam et al. 2006, 2004; Stam 2008). The reflected starlight can also be partly circularly polarized, because our model atmospheres contain not only Rayleigh-scattering gases but also cloud particles (see Section 2.2). While Rayleigh scattering alone does not circularly polarize light, light that has been scattered once and is linearly polarized can get circularly polarized when it is scattered by cloud particles. The circularly polarized flux V of a planet is usually very small (see Kemp & Wolstencroft 1971; Hansen & Travis 1974; Kawata 1978), in particular when integrated over the planetary disk (L. Rossi et al. 2017, in preparation). In the following, we therefore neglect V. This does not introduce significant errors in F, Q, and U (see Stam & Hovenier 2005).

We define the degree of linear polarization of the reflected light as

$$P = \frac{\sqrt{Q^2 + U^2}}{F}, \tag{2}$$

which is independent of the choice of reference plane. In case $U = 0$, which is true for planets that are mirror symmetric with respect to the reference plane, the direction of polarization can be included in the definition of the degree of polarization:

$$P_s = -Q/F. \tag{3}$$

If $U = 0$ and $Q < 0$, the light is polarized parallel to the reference plane and $P_s \geqslant 0$, whereas if $U = 0$ and $Q \geqslant 0$, the light is polarized perpendicular to the reference plane and $P_s < 0$.

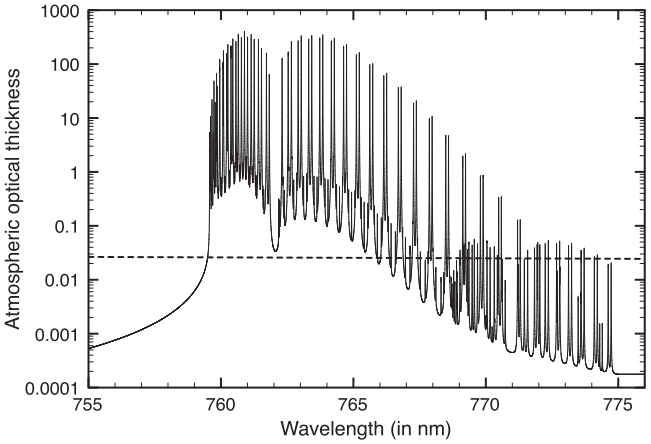

Figure 1. Solid line: gaseous absorption optical thickness of the Earth's atmosphere across the O_2 A-band, computed for a model atmosphere using a midlatitude summer pressure-temperature profile (McClatchey et al. 1972) and absorption-line parameters from Rothman et al. (2005). Dashed line: computed gaseous scattering optical thickness of the same model atmosphere. Its value decreases from 0.027 at 755 nm to 0.024 at 775 nm. Details on the absorption-line profiles and computation can be found in Stam et al. (2000b).

2.2. The Planetary Model Atmospheres and Surfaces

The atmospheres of our model planets are composed of stacks of locally horizontally homogeneous layers containing gas molecules and, optionally, cloud particles. We assume that the gas is terrestrial air and use pressure-temperature profiles representative of the Earth (McClatchey et al. 1972).

For our model planets, we calculate $b_{\rm abs}$, the gaseous absorption optical thickness of the atmosphere, as the integral of the mixing ratio η of the absorbing molecules times the gaseous number density (in m^{-2}) times the absorption cross-section $\sigma_{\rm abs}$ (in m^2) along the vertical direction. Both η and $\sigma_{\rm abs}$ usually depend on the ambient pressure and temperature, and thus on the altitude. Figure 1 shows the computed $b_{\rm abs}$ of the Earth's atmosphere across the wavelength region with the O_2 A-band, with a spectral resolution high enough to resolve individual absorption lines. We have calculated this $b_{\rm abs}$ following Stam et al. (2000b), assuming that O_2 is well-mixed, with $\eta = 0.21$. Note that $b_{\rm sca}$, the gaseous scattering optical thickness of the Earth's atmosphere, is about 0.0255 in the middle of the absorption band.

Figure 2 shows the flux and degree of linear polarization of unpolarized incident light that is singly scattered by a sample of gas molecules. Here, we use the Rayleigh-scattering matrix described by Hansen & Travis (1974) with a depolarization factor of 0.03. The depolarization factor modifies the isotropic Rayleigh-scattering matrix (that applies to molecules that are perfect dipoles) to that of most molecules found in planetary atmospheres, whose scattering exhibits some anisotropy (for details, see Young 1981). Although Figure 2 pertains to singly scattered light, we use the phase angle (i.e., $180 - \Theta$, where Θ is the single-scattering angle) to facilitate the comparison with planetary light curves later on.

The cloud particles are spherical and consist of liquid water with a refractive index of 1.335. The cloud particles are distributed in size according to a log-normal size distribution (see Equation (2.56) in Hansen & Travis 1974) with an effective radius of 6.0 μm and an effective variance of 0.5. We calculate the single-scattering properties of the cloud particles using Mie theory and the algorithm described by de Rooij & van der Stap (1984). Figure 2 shows the flux and degree of linear polarization of unpolarized incident light that is singly scattered by a sample of the cloud particles at $\lambda = 765$ nm. Because we only consider the 20 nm wide wavelength region of the O_2 A-band, we ignore any wavelength dependence of the single-scattering properties of cloud particles.

The surface below the atmospheres is locally horizontally homogeneous and reflects Lambertian, i.e., isotropic and unpolarized, with a surface albedo A_s. While our model atmospheres and surfaces are locally horizontally homogeneous, our model exoplanets can be globally horizontally inhomogeneous; for example, they can be covered by patchy clouds (see Section 3.3).

2.3. Integration Across the Planetary Disk

We perform the calculations of the starlight that is reflected by a spherical model planet with the same adding-doubling algorithm used by Stam (2008), except here we use a (more computing time–consuming) disk-integration algorithm that also applies to horizontally inhomogeneous exoplanets (e.g., those with patchy clouds). We integrate across the illuminated and visible part of the planetary disk as follows:

1. We divide the disk into equally sized square "detector" pixels. The more pixels, the higher the accuracy of the integration (especially for large phase angles) but the longer the computing time. We use 100 pixels along the planet's equator for every phase angle α. Numerical tests show that, with this number of pixels, convergence is reached at all phase angles.
2. For each pixel and a given α, we compute the illumination and viewing geometries for the location on the planet in the center of the pixel. The local illumination geometries are θ_0, the angle between the local zenith direction and the direction to the star, and ϕ_0, the azimuthal angle of the incident starlight (measured in the local horizontal plane). The local viewing geometries are θ, the angle between the local zenith direction and the direction to the observer, and ϕ, the azimuthal angle of the reflected starlight (measured in the local horizontal plane). For each pixel, we also compute β, the angle between the local meridian plane (which contains both the local zenith direction and the direction toward the observer) and the planetary scattering plane.
3. For each pixel, we then compute the locally reflected starlight with our adding-doubling algorithm and rotate this flux vector from the local meridian plane to the planetary scattering plane (Hovenier & van der Mee 1983). All rotated flux vectors are summed to obtain the disk-integrated flux vector. From that vector, the degree of polarization is obtained.

To avoid having to perform separate radiative transfer calculations for pixels with different illumination and viewing geometries but the same planetary atmosphere and surface, we calculate the (azimuthal angle–independent) coefficients of the Fourier series in which the locally reflected flux vector can be expanded (see de Haan et al. 1987) for a range of values of θ_0 and θ (because polarization is included, each coefficient is in fact a column vector) for every atmosphere-surface combination on a model planet. With these precomputed Fourier coefficients, we can efficiently evaluate the flux vector of the locally reflected starlight for each pixel and every α.

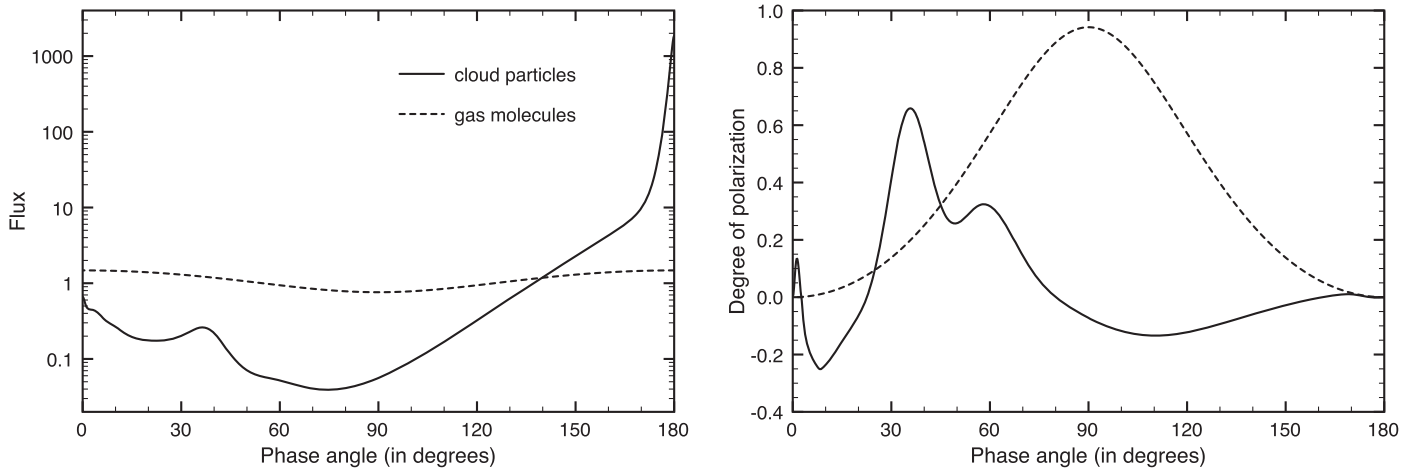

Figure 2. Total flux (left) and degree of linear polarization (right) of unpolarized incident light at $\lambda = 765$ nm that is singly scattered by samples of the cloud particles (solid lines) and of the Rayleigh-scattering gas molecules (dashed lines) as functions of the phase angle (i.e., 180°, the single-scattering angle). The flux and polarization peak around 35° in the cloud particle curves is the primary rainbow.

We normalize each disk-integrated flux vector such that the reflected total flux at $\alpha = 0°$ equals the planet's geometric albedo. With this normalization—and given the stellar luminosity, planetary orbital distance and radius, and distance between the planet and the observer—the absolute values of the flux vector arriving at the observer can be straightforwardly calculated (see Equations (5) and (8) of Stam et al. 2004). Because the degree of polarization is a relative measure, it is independent of the absolute fluxes.

2.4. Spectral Computations

When measuring starlight that has been reflected by an Earth-like exoplanet, the spectral resolution across a gaseous absorption band will likely be much lower than that shown in Figure 1. The most accurate simulations of low spectral resolution observations across a gaseous absorption band would require radiative transfer calculations at a spectral line–resolving resolution (so-called line-by-line calculations) followed by a convolution with the actual instrumental spectral response function. Performing line-by-line calculations while fully including polarization and multiple scattering for planets with cloudy atmospheres and integrating across the planetary disk for various phase angles requires several hours of computing time. Our approach to computing low spectral resolution spectra across the O_2 A-band is therefore based on the correlated *k*-distribution method (hereafter the c*k*-method).

A description of the c*k*-method without polarization was given by Lacis & Oinas (1991). The application of the c*k*-method for polarized radiative transfer has been described by Stam et al. (2000b). That paper also includes a detailed comparison between simulations using the line-by-line method and the c*k*-method to assess the accuracy of the latter. According to Stam et al. (2000b), the absolute errors in the degree of polarization across the O_2 A-band for sunlight that is locally reflected by cloudy, Earth-like atmospheres due to using the c*k*-method are largest in the deepest part of the band but still less than 0.0025 for a spectral bin width $\Delta\lambda$ of 0.2 nm (the line-by-line method yields a slightly stronger polarization in the band). The errors decrease with increasing $\Delta\lambda$ and are much smaller for cloud-free atmospheres because they arise due to scattering. In cloud-free Earth-like atmospheres, at these wavelengths, there is very little scattering.

For a given atmosphere-surface combination, we compute and store the Fourier coefficients of the locally reflected flux vectors for the range of atmospheric absorption optical thicknesses b_{abs} shown in Figure 1, i.e., from 0 (the continuum) to 400 (the strongest absorption line). We use the stored coefficients to efficiently calculate the reflected vector for the desired spectral bins $\Delta\lambda$ across the absorption band, given the distribution of b_{abs} in each spectral bin. The integration across each $\Delta\lambda$ is performed with Gauss-Legendre integration. We use a block function for the instrumental response function per spectral bin. As described in Stam et al. (2000b), the c*k*-method can be combined with other response functions. A block function, however, captures the variation across the band without introducing more free parameters.

Figure 3 shows the disk-integrated reflected flux F and degree of polarization P_s across the band of a cloud-free planet with a black surface for $\Delta\lambda$ ranging from 0.5 to 0.8 nm. The difference between F and P_s in the deepest part of the band and in the continuum decreases with increasing $\Delta\lambda$ as more wavelengths where b_{abs} is small fall within the spectral bin. This difference also depends on the O_2 mixing ratio; the presence, thickness, and altitude of the clouds; and the surface albedo (see Section 3 for a detailed explanation of the shapes of the curves). In the following, we use $\Delta\lambda = 0.5$ nm and 50 Gaussian abscissae per spectral bin (similar to what was used by Stam et al. 2000b).

3. Numerical Results

3.1. Cloud-free Planets

3.1.1. The Influence of the Surface Albedo A_s

The first results to discuss are those for starlight reflected by model planets with gaseous, cloud-free atmospheres above surfaces with different albedos. Figure 4 shows F and P_s for surface albedos A_s ranging from 0.0 to 1.0 at a phase angle α of 90°. This is a very advantageous phase angle for the direct detection of an exoplanet, because its angular distance to its host star is largest. This phase angle also occurs at least twice in every planetary orbit, independent of the orbital inclination angle.

For these cloud-free planets, F and P_s in the continuum depend strongly on A_s, because the atmospheric gaseous

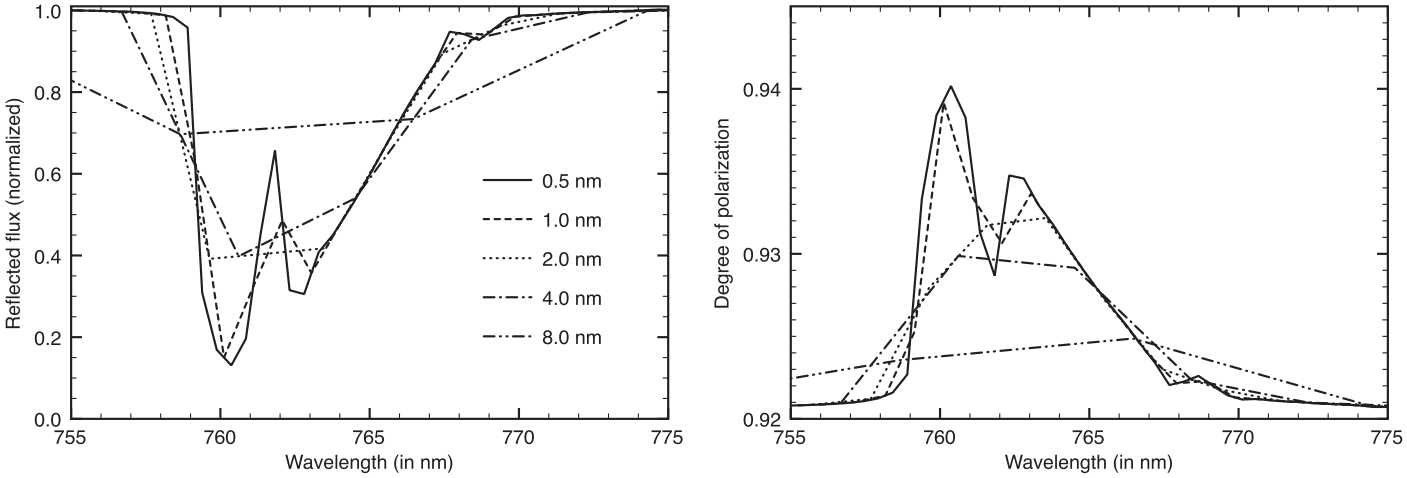

Figure 3. Flux F (left) and degree of polarization P_s (right) of starlight reflected by a cloud-free planet with a black surface at $\alpha = 90°$ for spectral bin widths $\Delta\lambda$ ranging from 0.5 to 0.8 nm.

scattering optical thickness b_{sca} in this spectral region is very small (see Figure 1). The continuum P_s decreases with increasing A_s because of the increasing contribution of unpolarized light that has been reflected by the surface to the planetary signal. Even if A_s is only slightly larger than zero, the surface contribution already strongly influences this signal.

For these cloud-free planets with gaseous atmospheres, polarization P_s will increase with increasing b_{abs} because the contribution of multiple scattered light—usually with a low degree of polarization—to the planetary signal will decrease. Also, at wavelengths where the atmospheric absorption optical thickness b_{abs} is large (see Figure 1), virtually no light will reach the surface to subsequently emerge from the top of the atmosphere. At those wavelengths, F and P_s are insensitive to A_s. In Figure 4, F and P_s in the deepest part of the absorption band (around 760.5 nm) depend on A_s. This occurs because every spectral bin includes wavelengths where b_{abs} is small and thus light that has been reflected by the surface.

In exoplanet observations, absolute fluxes (such as those shown in Figure 4) might not be available because of missing knowledge about, e.g., the planet radius and/or the distances involved. Such observations could, however, provide relative fluxes, as shown in Figure 5. For a cloud-free atmosphere, the relative depth of the absorption band appears to be very insensitive to A_s, provided $A_s > 0.0$ (the curve for $A_s = 0.05$, which is not shown in the figure, would fall only slightly above that for $A_s = 0.1$). The curves in Figure 5 pertain to horizontally homogeneous planets, but this insensitivity of the relative band depth to A_s also holds for cloud-free planets with a range of albedos across their surfaces.

This insensitivity of the relative band depth in flux can be explained by how the reflected flux varies with b_{abs}, shown in Figure 6. Because of the small values of b_{sca} in this spectral region, and thus the small amount of multiple scattering, the flux that reaches the surface and then the top of the atmosphere depends almost linearly on A_s for every value of b_{abs}. The insensitivity is thus independent of the spectral resolution. The slight increase of the relative band depth with increasing A_s visible in Figure 5 is due to the slight increase in multiple scattered light and hence a slight increase in absorption. With a higher surface pressure, and thus a larger b_{sca} and more multiple scattering, the relative band depth will show a larger sensitivity to A_s.

Figure 6 also shows that, in polarization spectra, the widths of individual absorption lines decrease with increasing surface albedo A_s. The explanation for this narrowing of absorption lines in polarization spectra is that if for a given value of b_{abs}, A_s is increased, more unpolarized light is added to the reflected starlight, decreasing P_s (see Equation (13) in Stam et al. 1999).

3.1.2. The Influence of the Planetary Phase Angle α

Figure 7 shows F and P_s in the continuum (755 nm) as functions of the planetary phase angle α for different values of A_s. For comparison, the curves for $b_{abs} = 400$ (the deepest absorption lines in the O_2 A-band) are also shown (F is virtually zero). These curves (that are independent of A_s) can be used to estimate the expected strength of individual absorption lines as compared to the continuum.

The continuum F decreases smoothly with increasing α, while the continuum polarization curves have a maximum that shifts from 90° when the surface is black to larger values of α with increasing A_s. Both for the planet with the black surface and for the planet with $b_{abs} = 400$, P_s peaks at or near $\alpha = 90°$, because for those planets the signal is mostly determined by light singly scattered by gas molecules (there is almost no multiple scattering in the atmosphere, and there is no contribution from the surface). In addition, at that phase angle, the scattering angle of the singly scattered light is 90°, precisely where Rayleigh-scattered light has the highest polarization (see Figure 2). At 755 nm, the model atmosphere has a very small gaseous scattering optical thickness, the reflected flux is thus mainly determined by A_s, and the maximum of P_s decreases rapidly with increasing A_s and shifts to larger values of α.

From the polarization curves in Figure 7, it can be seen that, for cloud-free planets with reflecting surfaces, the polarization inside the absorption band will be higher than that in the continuum at all phase angles. For black planets and $60° < \alpha < 90°$, the P_s should be slightly lower inside the deepest absorption lines than it is in the continuum. However, as can be seen in Figure 6, showing the flux and P_s as functions of b_{abs} at $\alpha = 90°$ for various values of A_s, lower values of P_s will only occur in the deepest absorption lines (where the flux is extremely small). Thus, for cloud-free planets without an absorption line–resolving spectral resolution, the P_s in the band

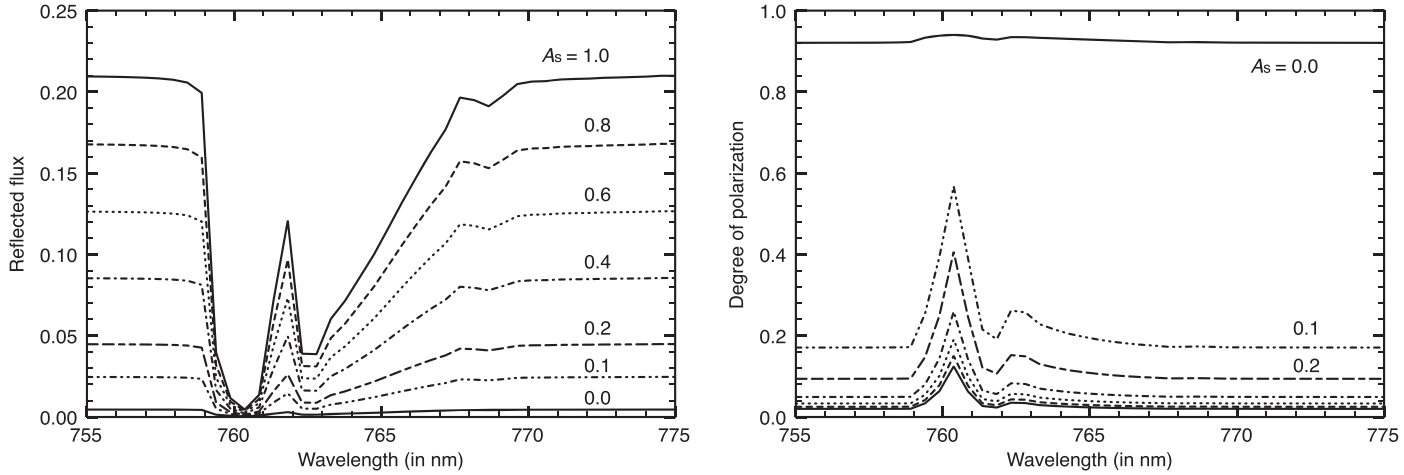

Figure 4. Flux F (left) and degree of polarization P_s (right) of starlight reflected by cloud-free exoplanets at $\alpha = 90°$ for different surface albedos A_s: 0.0 (thin solid line; cf. Figure 3 and note the different polarization scale), 0.1 (dot-dot-dashed line), 0.2 (short-long-dashed line), 0.4 (dot-dashed line), 0.6 (dotted line), 0.8 (dashed line), and 1.0 (thick solid line).

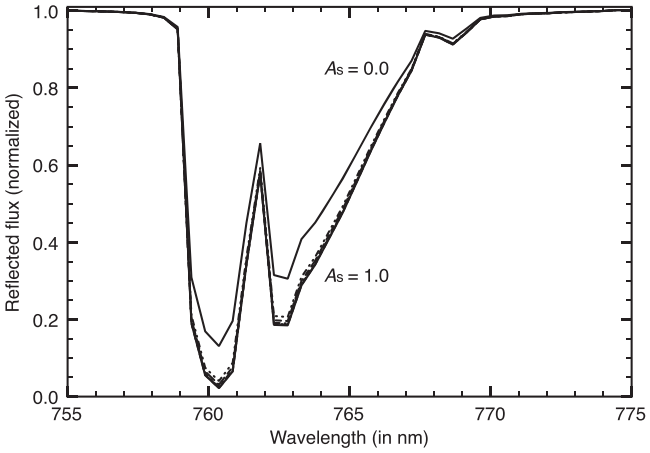

Figure 5. Reflected flux curves of Figure 4 normalized at $\lambda = 755$ nm. The shallowest band pertains to $A_s = 0.0$ and the deepest to $A_s = 1.0$.

is expected to be higher than that in the continuum at all phase angles and for all A_s.

3.1.3. The Influence of the Mixing Ratio η

The strength of the O_2 A-band for a cloud-free atmosphere also depends on the O_2 mixing ratio η. Figure 6 gives insight into the influence of η because b_{abs} depends linearly on η (for a given surface pressure). To better illustrate the observable signals, Figure 8 shows F and P_s in the spectral bin covering the deepest part of the absorption band (around 760.4 nm) for η up to 1.0 (a pure O_2 atmosphere) as functions of A_s. The curve for $\eta = 0.0$ equals the continuum. The phase angle is 90°.

The reflected flux curves in Figure 8 show that (1) the band depth (i.e., the 1.0 curve) increases with increasing η, with saturation starting for $\eta > 0.4$ independent of A_s; and (2) the insensitivity of the band depth to A_s (see Figure 5 for $\eta = 0.21$) holds for all values of η except when the surface is (near) black. The polarization curves show that, with the 0.5 nm wide spectral bin, the band strength (i.e., |curve–continuum|, with the continuum P_s given by the solid line in Figure 8) is smallest when the surface is near-black for all η.

For a cloud-free planet with a depolarizing surface, high polarization is usually associated with low fluxes. The relation between the band strength in P_s and the band depth in the normalized F, derived from Figure 8, is shown in the top left panel of Figure 9 (data for $\eta = 0.0$ have been omitted). The plot clearly shows that the band depth in F is most sensitive to A_s when the surface is dark ($A_s < 0.1$) and η is small. Also, large polarization band strengths (>0.5) correlate with large band depths in F. Indeed, if one were to measure a large band strength in P_s combined with a small band depth in F, one would have an indication that the planetary atmosphere contains clouds and/or haze particles in addition to gaseous molecules (see Section 3.2).

The data points in Figure 9 have been calculated assuming an Earth-like surface pressure and thus an Earth-like value for b_{sca}. Calculations show that data points for other (still small) values of b_{sca} fall between those shown in Figure 9. For a surface pressure (and hence b_{sca}) twice as high as the Earth's, the data points for, e.g., $\eta = 0.2$ are similar to those for $\eta = 0.4$, except for slightly different values of A_s. Thus, measuring a certain combination of band strength in P_s and band depth in F without knowing the surface pressure and A_s would not directly allow the retrieval of η.

3.2. Completely Cloudy Planets

3.2.1. The Influence of the Cloud Optical Thickness b_{cloud}

The Earth has an average CC of about 60%, with cloud optical thicknesses b_{cloud} ranging from almost 0 to over 100 in the visible (Marshak & Davis 2005). Figure 10 shows the influence of b_{cloud} on F and P_s in the continuum around the O_2 A-band as functions of α for $A_s = 0.0$. These curves show the background on which the absorption band could be measured. The cloud is a horizontally homogeneous layer that is 2 km thick with its top at 6 km, embedded in the gaseous atmospheres discussed in Section 3.1.

The curves in Figure 10 show how increasing b_{cloud} brightens a planet at all phase angles, except for optically thin clouds ($b_{cloud} \leqslant 1.0$), where the planets are darkest at $60° < \alpha < 90°$. This is due to the single-scattering phase function of the cloud particles (Figure 2). This single-scattering phase function is also the explanation for the "primary rainbow": the shoulder in F and the local maximum in P_s around $\alpha = 38°$. The rainbow feature could help to identify

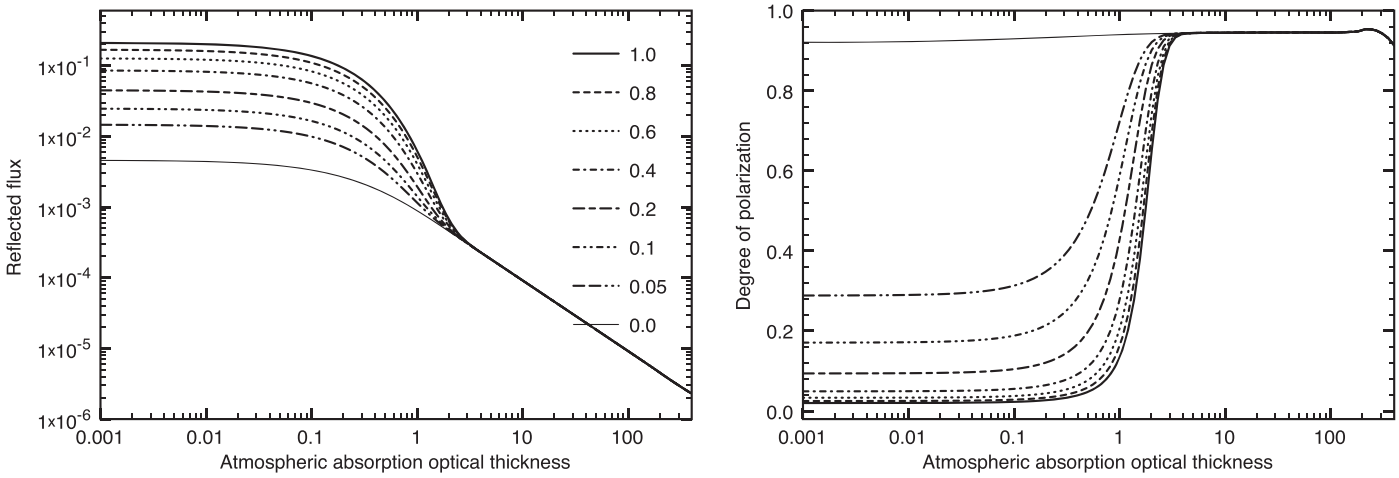

Figure 6. The F (left) and P_s (right) of starlight reflected by cloud-free exoplanets at $\alpha = 90°$ as functions of b_{abs} for different values of A_s.

water clouds on exoplanets (see, e.g., Karalidi et al. 2012; Bailey 2007).

The Rayleigh-scattering polarization maximum around 90° disappears with increasing b_{cloud}, as the scattering by the cloud particles increasingly dominates the reflected signal. In particular, around $\alpha = 90°$, the single-scattering polarization of the cloud particles is almost zero (see Figure 2). At small phase angles, the P_s of the cloudy planets is negative, and the polarization direction is thus parallel to the reference plane. The directional change from parallel to perpendicular to the reference plane occurs around $\alpha = 20°$. Another directional change occurs at a larger phase angle: the larger the b_{cloud}, the closer this phase angle is to 80° for the liquid water particles that form our clouds (see Figure 2).

Figure 11 shows F (normalized at 755 nm; for the absolute differences in the continuum flux, see Figure 10) and P_s across the O_2 A-band for the same model planets at $\alpha = 90°$. The flux band depth depends only weakly on b_{cloud} because of two opposing effects: (1) increasing b_{cloud} decreases the average photon path length (and thus the absorption) because more photons are scattered back to space, and (2) increasing b_{cloud} increases the average photon path length (and thus the absorption) through the increase of multiple scattering in the atmosphere. Which effect dominates depends on the values of b_{abs} within a spectral bin, the illumination and viewing geometries, and the cloud micro- and macrophysical properties. For our model planets, the net effect is a flux band depth that is insensitive to b_{cloud}.

This insensitivity holds for any O_2 mixing ratio η, as can be seen in Figure 12, where we plot F and P_s in the spectral bin covering the deepest part of the band as functions of b_{cloud} and η. Indeed, for $b_{cloud} > 1.0$ and $\eta > 0.2$, the flux band depth is fairly constant with b_{cloud} for every η. Because of the insensitivity to b_{cloud}, η could be derived from the band depth of the normalized flux, although we would have to know the cloud-top altitude (see Section 3.2.2).

The strength of the absorption band in P_s is sensitive for b_{cloud} up to about 5 (for larger b_{cloud} and $\eta = 0.21$, the band has virtually disappeared). The continuum P_s decreases with increasing b_{cloud} (see also Figure 10). The P_s in the band also decreases, but at a different rate: at wavelengths where b_{abs} is large, the clouds will be invisible and P_s will be high (see the $b_{abs} = 400$ line Figure 7), while at wavelengths with little absorption, P_s will behave similarly to that in the continuum. With unresolved absorption lines, as in Figure 11, the band strength is a mixture of high and low polarization. According to Figure 12, the P_s band strength (the absolute difference between each curve and the $\eta = 0.0$ curve) increases with increasing η, yielding band strengths of tens of percent in P_s.

Figure 9 includes a scatter plot based on Figure 12 that shows the relation between the P_s band strength and the (normalized) F band depth for various b_{cloud} values. Large P_s band strengths clearly correlate with large F band depths. Thus, measuring a strong P_s band in combination with a shallow F band at $\alpha = 90°$ would not be explainable by a cloud layer of liquid water particles. A reflecting surface, instead of $A_s = 0.0$, would decrease P_s even more (except for very thick clouds, where A_s is irrelevant) and would thus not improve the explanation.

The previous discussion focused on $\alpha = 90°$. It can be seen from Figure 10 that, around $\alpha = 38°$, the continuum P_s of planets with optically thin clouds is higher than that of a cloud-free black planet. Because with increasing b_{abs} the signals of all planets tend toward those of cloud-free planets, the P_s inside the deepest lines of the O_2 A-band could be lower than in the weaker lines and the continuum for dark—e.g., ocean-covered—planets with thin clouds, around $\alpha = 38°$. This can be seen in Figure 13.

When absorption lines are not resolved, the effect will be smaller than that shown in Figure 13, because wavelengths with large b_{abs} will be mixed with wavelengths with small b_{abs}. Figure 14 shows the band in P_s with our spectral bin width of 0.5 nm at $\alpha = 38°$. For $b_{cloud} = 0.5$, the P_s in the spectral bins with the strongest absorption lines is indeed lower than that in the adjacent bins, creating a band with a collapsed top. A nonzero surface albedo will lower the continuum P_s for planets with optically thin clouds and diminish this inversion in the O_2 A-band. Figure 14 also shows the lack of a band feature on a cloud-free planet with a dark surface (because of the small b_{sca}) and the difference in P_s between a planet with a thick cloud ($b_{cloud} = 50.0$) and a cloud-free planet with a white surface, which will have similar fluxes.

Figure 13 also shows that the widths of the resolved absorption lines depend on b_{cloud}. In F, optically thicker clouds narrow the lines for $0.1 \leqslant b_{abs} \leqslant 10$ as compared to those in the spectra of cloud-free planets. In P_s, the lines can exhibit various shapes: narrowed (for $b_{cloud} = 50.0$), widened with a tiny dip (0.01 or 1%) when $b_{abs} > 4$ (for $b_{cloud} = 5.0$), or with

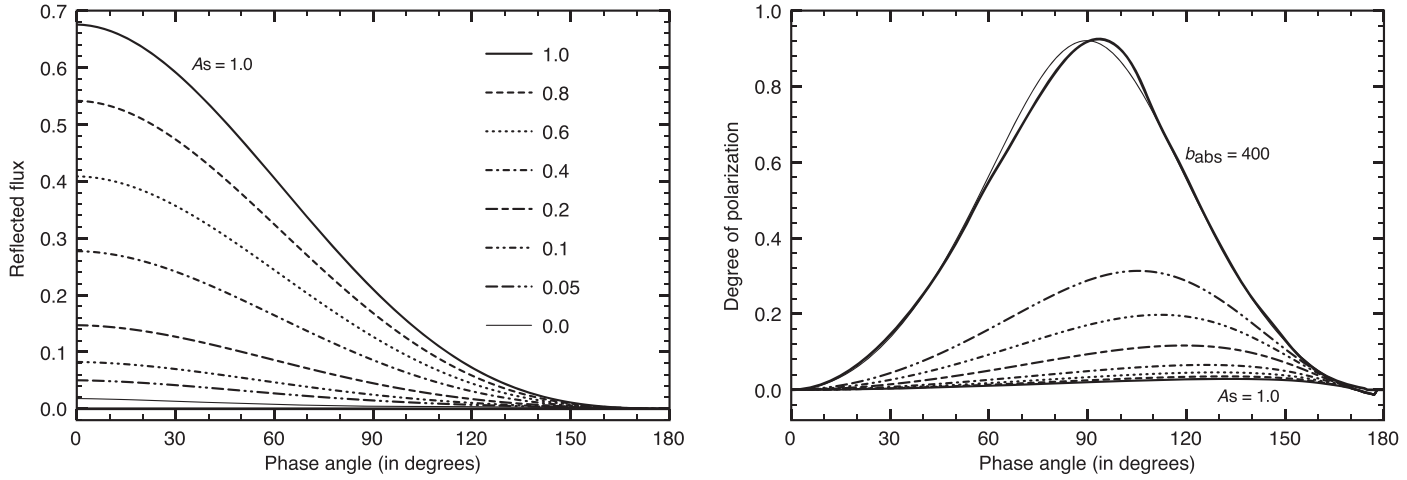

Figure 7. The F (left) and P_s (right) of starlight reflected at $\lambda = 755$ nm (the continuum) by cloud-free exoplanets as functions of α for the same A_s as in Figure 4, but with curves for $A_s = 0.05$ added. The thick solid curve peaking at $\alpha = 93°$ in P_s (F is virtually zero) pertains to $b_{abs} = 400$.

higher P_s (0.02 or 2%) at the edges with a narrow dip starting at $b_{abs} \approx 0.6$. The precise values of b_{abs} mentioned above depend on α, as can be seen when comparing the curves for the cloud-free planet in Figure 13 (with $\alpha = 38°$) with those in Figure 6 (where $\alpha = 90°$). Examples of variations of line shapes in P_s in the presence of aerosol can be found in Stam et al. (1999).

3.2.2. The Influence of the Cloud-top Altitude z_{top}

Because on Earth the mixing ratio of O_2 is well known and more or less constant with altitude, the depth of the O_2 A-band in the flux that is reflected to space can be used, to a first approximation, to derive the altitude of the top of a cloud layer. Indeed, this is the basis of several cloud-top altitude retrieval techniques (Fischer & Grassl 1991; Fischer et al. 1991). In this section, we investigate the relation between cloud-top altitude, z_{top}, and band depths and strengths for our model planets.

Figure 15 shows the (normalized) F and P_s across the O_2 A-band for exoplanets with black surfaces that are completely covered by horizontally homogeneous clouds with $b_{cloud} = 10$ and z_{top} ranging from 2.0 to 10.0 km. The figure shows that the higher the cloud, the shallower the band in F. This is to be expected, because the higher the cloud, the shorter the mean photon path through the atmosphere, and thus the less absorption. For the lowest cloud, the lowest (normalized) F is only 6% of the continuum. For the highest cloud, it is almost 20% of the continuum. Interestingly, the F band depth for the cloud-free planet is similar to that for a cloudy planet with $z_{top} = 6$ km. Because, for the cloud-free planet with $A_s = 0.0$, only Rayleigh scattering contributes, its absolute flux will of course be much smaller than that of the cloudy planet (see Figure 10). A cloud-free planet with $A_s = 1.0$ that would have an absolute flux similar to that of a cloudy planet would have an F band depth similar to that of the planet with $z_{top} = 2$ km (see Figure 5).

The continuum P_s decreases with z_{top} and changes from perpendicular to parallel to the reference plane when z_{top} exceeds about 7 km (this altitude will depend on b_{cloud}). The negative P_s is due to the negative single-scattering polarization of the cloud particles at $\alpha = 90°$ (see Figure 2), and the higher the clouds, the stronger their contribution to the planetary P_s. Measurements by the POLDER instrument (Deschamps et al. 1994) of the continuum polarization of sunlight reflected by regions on Earth are indeed being used to derive cloud-top altitudes (Goloub et al. 1994; Knibbe et al. 2000), and a similar approach was used for cloud-top altitude retrieval on Venus using Pioneer Venus orbiter data and sulfuric acid model clouds (Knibbe et al. 1998). Because of the abundance of photons in these Earth and Venus observations, high polarimetric accuracies can be reached. For example, the accuracy of POLDER is about 0.02 in degree of polarization (Toubbé et al. 1999).

The cloud-top altitude also affects the P_s in the band: the higher the cloud, the shallower the band. The reason for this change in band strength is that, with increasing z_{top}, the absorption optical thickness above the cloud decreases. While the P_s in the deepest absorption lines will remain high, it will decrease in the wings of these lines; see Figure 14 for $\alpha = 38°$ (for optically thin clouds, it will increase when $\alpha = 38°$).

The effect of the O_2 mixing ratio η on F and P_s in the spectral bin covering the deepest part of the O_2 A-band for various values of z_{top} is shown in Figure 16 (recall that the continuum F and P_s equal the case for $\eta = 0.0$, only shown in the polarization plot). On Earth, the tops of optically thick clouds will usually not have a z_{top} higher than about 14 km (except at equatorial latitudes, where the tropopause can reach altitudes of about 18 km), but because cloud formation depends strongly on the atmospheric temperature profile, which depends on the planet, we have included larger values for z_{top}. It can be seen how the band depth in F decreases with increasing z_{top}: for $\eta > 0.5$, the F in the band is close to zero unless $z_{top} > 10$ km and thus insensitive to z_{top}. There is an ambiguity between z_{top} and η: an observed band depth in F could be fitted with different combinations of z_{top} and η. The band strength in P_s (i.e., the difference between the nonsolid curves and the solid, $\eta = 0.0$, curve) decreases with increasing z_{top} and is close to zero for small values of η and/or $z_{top} > 12$ km. Here there is a similar ambiguity, except that the smaller the η, the smaller the maximum band strength in P_s: large band strengths can only be explained by large η values and/or low clouds.

The band strength in P_s as a function of the band depth in (normalized) F is also shown in the bottom left panel of Figure 9. This figure makes clear that measuring both the band depth in F and the band strength in P_s would allow the

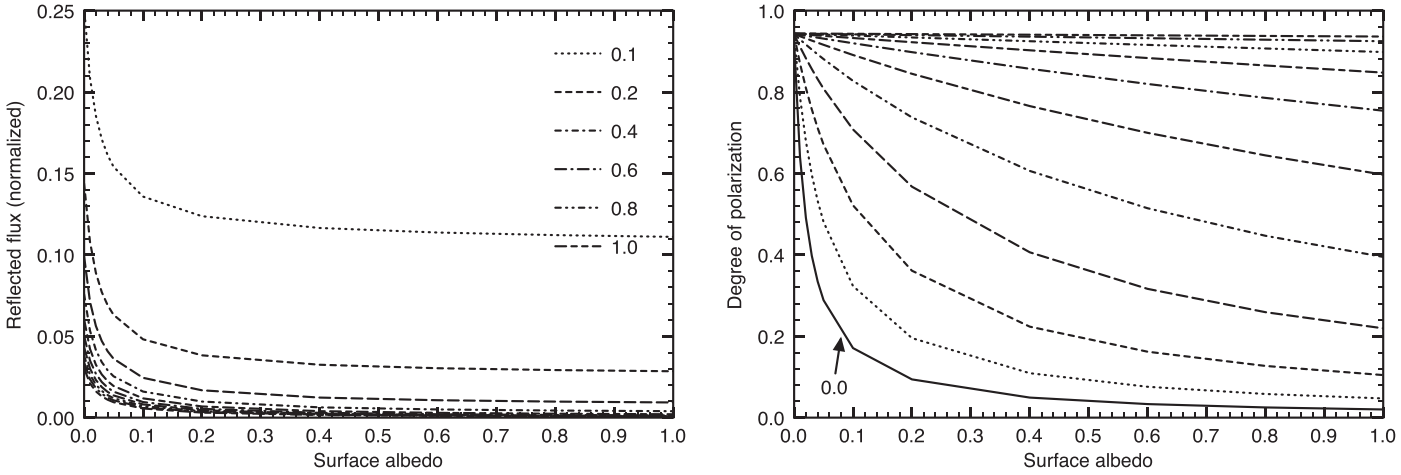

Figure 8. The F (left; normalized to its continuum value) and P_s (right) of starlight reflected by cloud-free exoplanets in the deepest part of the O_2 A-band (the spectral bin around $\lambda = 760.4$ nm) at $\alpha = 90°$ as functions of A_s for η ranging from 0.0 (thick solid line, not shown in the flux as it equals 1.0) to 1.0 (long-short-short-long-dashed line) in steps of 0.1. The short-dashed line represents $\eta = 0.2$, closest to the Earth's value.

retrieval of both z_{top} and η, although that would require very accurate measurements and (in the absence of absolute flux and polarization measurements) assumptions about the CC and the planet's surface albedo, especially with small values of b_{cloud}.

3.3. Partly Cloudy Planets

The model planets that we used previously were either cloud-free or fully covered by a horizontally homogeneous cloud layer. These planets provide straightforward insight into the influence of clouds on the depth and strength of the O_2 A-band in, respectively, flux and polarization. The bottom right panel of Figure 9 contains all the data points of the other panels and thus shows the band strength in P_s as a function of the band depth in F for different values of A_s, η, b_{cloud}, and z_{top}. The cloud of data points in this panel shows that the larger the value of η, the larger the possible range of band depths in F and band strengths in P_s, and that for an Earth-like η of 0.21, the band will show up in P_s only for dark (but not too dark) surfaces and optically thin clouds ($b_{cloud} < 5.0$) (at $\alpha = 90°$ and with our spectral bin width of 0.5 nm). A horizontally homogeneous planet is, however, an extreme case. Here, we will use horizontally inhomogeneous model planets with patchy surfaces and patchy clouds, such as those found on Earth.

For our horizontally inhomogeneous model planets, we use the following values for the surface albedo A_s: 0.90 (representative of fresh snow), 0.60 (old and/or melted snow), 0.40 (sandy lands), 0.25 (grassy lands), 0.15 (forests), and 0.06 (oceans). Figure 17 shows an example of a (pixelated) cloud-free model planet at $\alpha = 90°$ covered by six types of surfaces. The geometric albedo of this planet is 0.24.

All of our surfaces are depolarizing; thus, we do not include, e.g., Fresnel reflection to describe the ocean surface. In Stam (2008), the disk-integrated signal of a cloud-free Earth-like planet with a flat Fresnel-reflecting interface on top of a black surface (including glint) was found to have a P_s that was about 0.04 lower than that of the same planet without the Fresnel-reflecting interface. For fully cloudy planets ($b_{cloud} = 10$), there was virtually no difference in the disk-integrated P_s. Waves on the ocean surface would very likely reduce the influence of the Fresnel reflection because of the randomizing effect of the variation in their directions, shapes, and heights.

To model a patchy cloud pattern, we choose a CC, i.e., the fraction of pixels that are cloudy. Note that these pixels are smaller than the pixels shown in Figure 17. Next, we distribute an initial number of cloudy pixels (iCC, where iCC is much smaller than the total number of cloudy pixels) randomly across the planetary disk. The remaining cloudy pixels are distributed across the remainder of the disk with the probability that a pixel will be cloudy increasing with the number of cloudy neighboring pixels. This method allows us to create patchy clouds with the size of the patches depending on the values of CC and iCC. In particular, the larger the difference between iCC and CC, the larger the patches. The user can assign different cloud properties (b_{cloud}, z_{top}, geometrical thickness, and particle microphysics) to different cloudy pixels.

Figure 18 shows the F and P[4] of the heterogeneous model planet shown in Figure 17 with CCs equal to 0.0 (cloud-free), 0.5, and 1.0 (completely cloudy). The cloud properties are given in the figure caption. Not surprisingly, the F of the fully cloudy planet is higher than that of the cloud-free planet. The lowest F is that of the partly cloudy planet, where one would expect a value in between the fluxes of the two other planets. Upon closer inspection, however, it appears that the poles of the partly cloudy planet are (partly) covered by clouds, suppressing F, because the clouds are less bright than the snow and ice surfaces. The polarization signal of the partly cloudy planet is between those of the other planets, because the polar regions do not contribute a significantly different polarization signal compared to the clouds.

As shown in Figure 9, horizontally homogeneous planets present a wide variation in band strengths in P versus band depths in F. Next, we will look at the variation that can be expected for horizontally inhomogeneous planets. In contrast to the curves in Figure 18, which have been computed for a horizontally inhomogeneous planet with patchy clouds and surface albedo, we will compute the variation of band strengths and depths by taking weighted sums of horizontally homogeneous planets to limit the computation times while maximizing the variations. Karalidi & Stam (2012) investigated the differences between "true" horizontal inhomogeneities and the weighted sum approach. While for individual planets, the

[4] For horizontally heterogeneous planets, the disk-integrated U is not necessarily equal to zero, and we therefore use P (Equation (2)) instead of P_s.

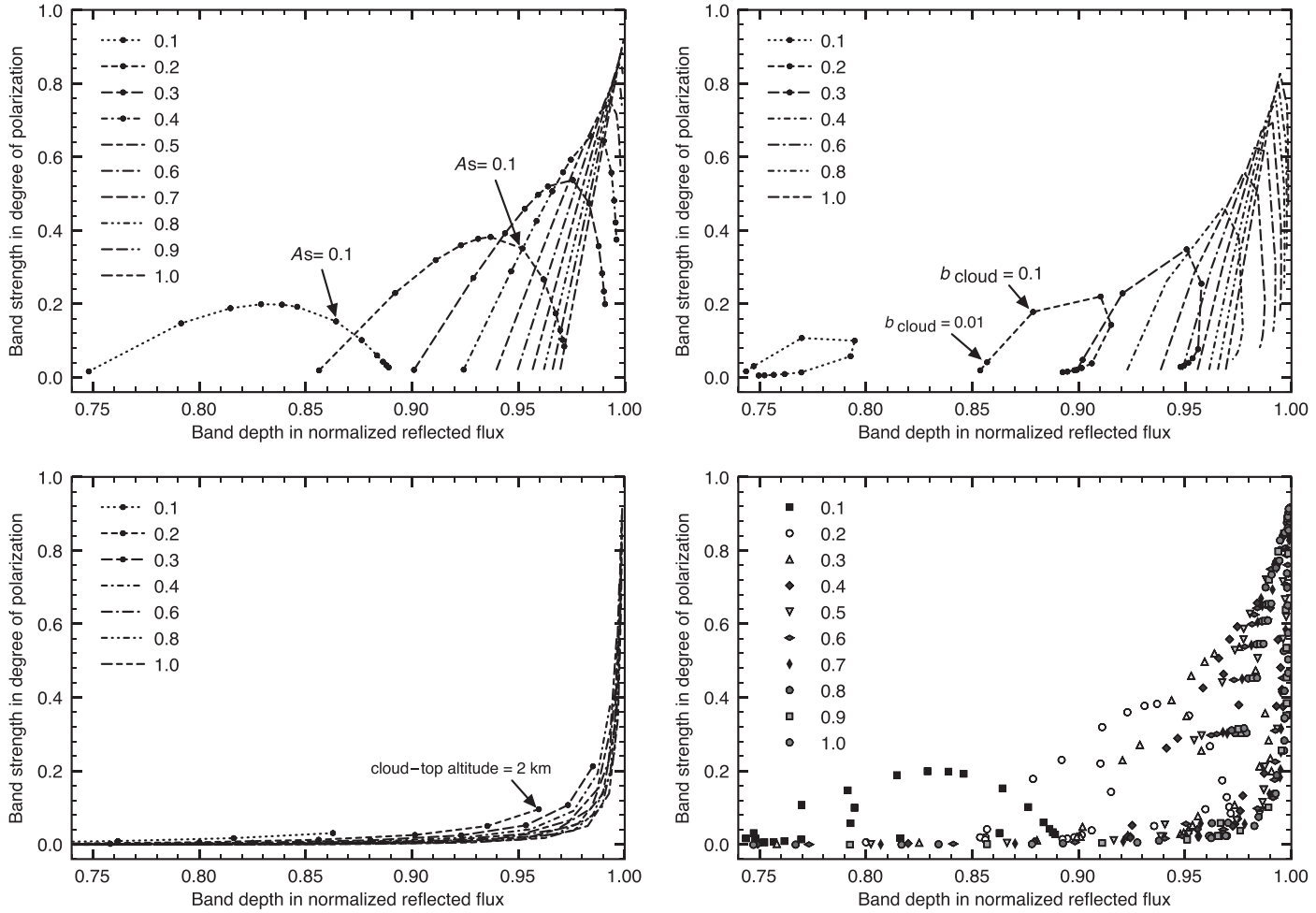

Figure 9. Scatter plot of ΔP vs. ΔF, with $\Delta P = P_{760.4\,\mathrm{nm}} - P_{755\,\mathrm{nm}}$ and $\Delta F = 1.0 - F_{760.4\,\mathrm{nm}}/F_{755\,\mathrm{nm}}$ (where $F_{\mathrm{x\,nm}}$ indicates the flux in the spectral bin around x nm). Data is shown for η ranging from 0.1 to 1.0 in steps of 0.1 (not all values appear in all legends). Top left: data points derived from Figure 8, thus for A_s equal to 0.0 (on the left of each line), 0.01, 0.02, 0.03, 0.04, 0.05, 0.1, 0.2, 0.4, 0.6, 0.8, and 1.0 (on the right of each line). Top right: data points derived from Figure 12, thus for b_{cloud} equal to 0.0 (on the left of each line), 0.01, 0.1, 0.5, 1.0, 5.0, 10.0, 50.0, and 100.0. Bottom left: data points derived from Figure 16, thus for cloud-top altitudes equal to 2.0 (on the right of each line), 4.0, 6.0, 8.0, 10.0, and 12.0 km (on the left of each line; note that we did not include flux band depths <0.74). Bottom right: all data points from the other three plots combined.

differences can be significant, both methods yield the same results statistically.

For a given value of η, we thus compute the flux vector of a planet using $\pi\boldsymbol{F} = (1/7)\Sigma_i^7 \pi\boldsymbol{F}_i$, where $\boldsymbol{F}_i$ is the flux vector of a horizontally homogeneous planet. The horizontally homogeneous planets used for the modeling can be either without clouds or completely covered by one of six cloud types. Table 1 shows the properties of the six cloud types. Types 1–5 consist of the same liquid water cloud particles that we used before. Type 6 consists of water ice crystals with scattering properties taken from Karalidi et al. (2012). We use the six surface albedos A_s specified in the caption of Figure 17 and, as before, assume Lambertian surface reflection, because we are mainly interested in the effects of the clouds and because the influence of a polarizing surface, such as a Fresnel reflection, is relatively small (Stam 2008).

To avoid ending up with a huge number of data points, we use a single value for A_s for each model planet, which still gives us 10,348 flux vectors of planets. Figure 19 shows data points for $\eta = 0.1$, 0.2, and 0.4. Several data points can be seen to line up, in particular those for cloud-free planets and planets with ice clouds. These lines of data points pertain to the "transition" from a homogeneous planet with a given surface albedo without clouds to a homogeneous planet with the same surface albedo but with clouds, with partially cloudy planets in between. Planets with optically thin clouds would fill the region between the densest part of the cluster of data points and the high P points for the planets without clouds and with ice clouds (see also Figure 9).

The data points in Figure 19 clearly illustrate the variation of the band depth in F for a single value of η due to the differences in A_s and the cloud types. Although increasing η generally increases the band depth in F, there is a huge overlap of data points for different values of η. When relatively small band depths in F are observed, however, one would know that η is small, even without knowledge of the presence of clouds and their properties or A_s.

The vertical extent of the data points in Figure 19 is a measure of the added value of measuring the band strength in P. The band strength could provide extra information about b_{cloud}, the CC, and A_s, in particular for optically thinner clouds. As can be seen, for higher values of η, the range of band strengths and thus the added value of P increases strongly at this phase angle of 90°. Conversely, large band strengths in P combined with large band depths in F would indicate high values of η.

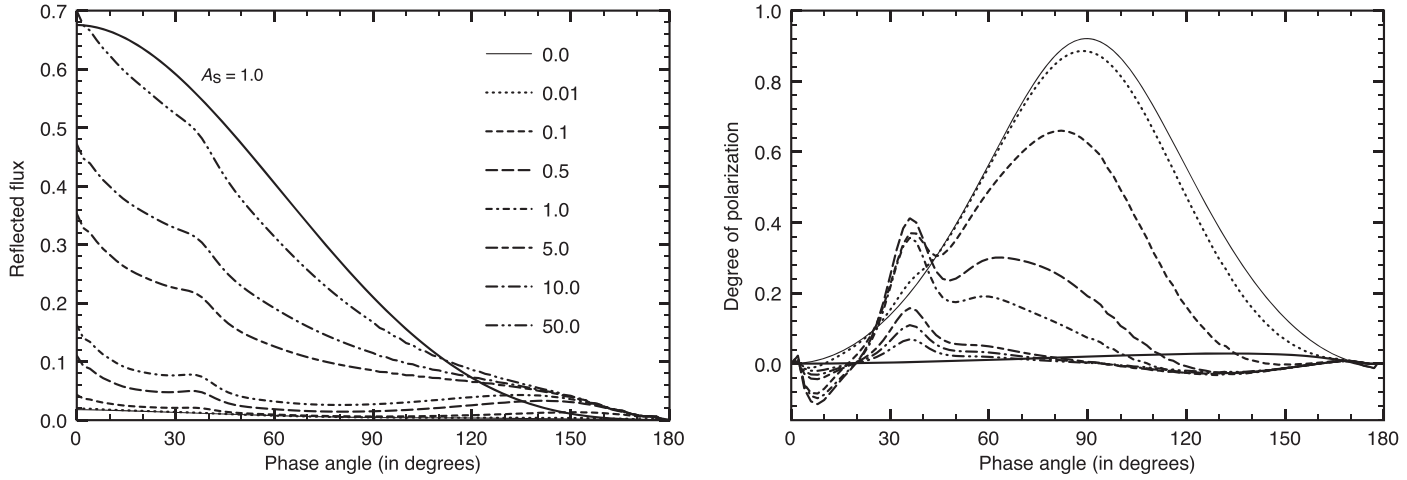

Figure 10. The F (left) and P_s (right) of starlight reflected at $\lambda = 755$ nm (the continuum) by completely cloudy exoplanets with $A_s = 0.0$ as functions of α. The optical thickness b_{cloud} (defined at 765 nm) varies from 0.01 to 50.0. The curves for the cloud-free planets ($b_{cloud} = 0.0$) with a black and a white surface ($A_s = 1.0$) are also included. The cloud layer extends from 4 to 6 km.

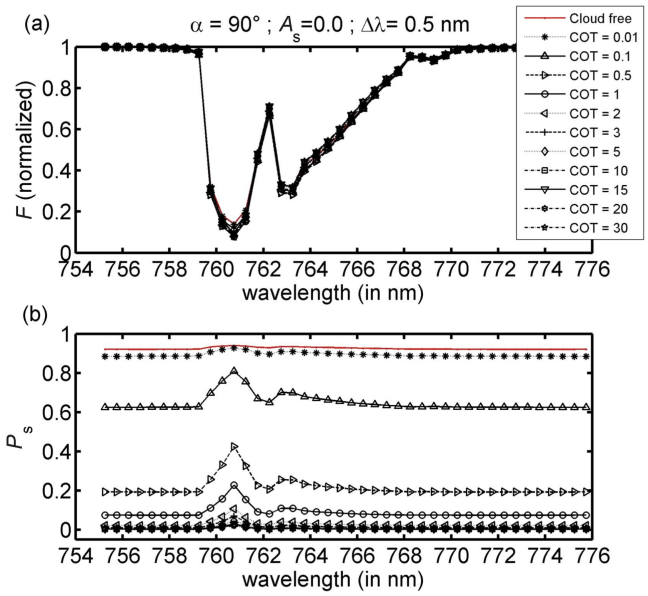

Figure 11. The F (top) and P_s (bottom) of starlight reflected by exoplanets that are completely covered by clouds from 4 to 6 km of altitude with cloud optical thicknesses (defined at 765 nm) ranging from 0.0 (cloud-free) to 30. The flux curves have been normalized at 755 nm.

The model planets that provide the data points for Figure 19 are quasi-horizontally inhomogeneous: their F and P values are representative of horizontally inhomogeneous planets, but they do not account for, e.g., the effects of localized and patchy clouds (the spectra in Figure 18 do account for these effects). In Figure 20, we illustrate the variation in the band depth in F and the band strength in P for planets with homogeneous surfaces ($A_s = 0.15$ or 0.6) and patchy clouds of types 1, 5, and 6 (the ice clouds). Each planet has one type of cloud. Given a planet with a certain CC, we compute F and P for 200 randomly selected shapes and locations of cloud patches (this method is described in detail in Rossi & Stam 2017). The error bars indicate the 1σ variability in the computed signals for each planet (the variability equals zero for the fully cloudy planets).

Figure 20 shows that, for a given CC and type, the actual distribution of the clouds across the planetary disk usually also influences the bands in F and P. The variability decreases with increasing CC because a large amount of clouds allows less spatial variation. Above a dark surface ($A_s = 0.15$), high-altitude, liquid water clouds with $b_{cloud} = 10$ (type 5, bottom left panel) show a smaller variance in both P and F than thin, low-altitude clouds (type 1, top left panel). Increasing the surface albedo of the latter planet (top right panel) decreases the variability in both P and F for all CCs while not strongly changing the average values. The spatial distribution of the thin, high-altitude ice clouds (type 6, bottom right panel) has a negligible influence on the bands for every η.

The large number of free parameters on a planet introduces significant degeneracies in the relation between band depths in F and band strengths in P. A detailed investigation of the data points and the underlying planet models as shown in Figures 19 and 20, not only at $\alpha = 90°$ but also at other phase angles and across a wider wavelength region (in particular, including shorter wavelengths that are more sensitive to the gas above the clouds), could lead to the development of a retrieval algorithm for future observations but is outside the scope of this paper.

4. Discussion

The detection of absorption bands and the subsequent determination of column densities or mixing ratios of atmospheric biosignatures such as O_2, H_2O, and CH_4 are crucial tools in the search for habitable environments and life on exoplanets. The strength of a gaseous absorption band in a visible planetary spectrum depends on the mixing ratio of the gas under investigation, other atmospheric constituents and vertical structure, and the surface properties.

On Earth, oxygen arises from large-scale photosynthesis and is well mixed up to high altitudes. Because we have detailed knowledge about the Earth's O_2 mixing ratio and vertical distribution, a routine Earth-observation method for determining cloud-top altitudes is the measurement of the depth of the O_2 A-band in the flux of sunlight that is reflected by completely cloudy regions (see Saiedy et al. 1965; Vanbauce et al. 1998; Koelemeijer et al. 2001; Preusker et al. 2007; Lelli et al. 2012; Desmons et al. 2013, etc.). Knowledge of cloud-top altitudes is important for climate studies and for determining the mixing ratios of gases such as ozone, H_2O, and CH_4 that are strongly altitude-dependent and whose spectral signatures are affected by the presence and properties of clouds. For exoplanets, cloud

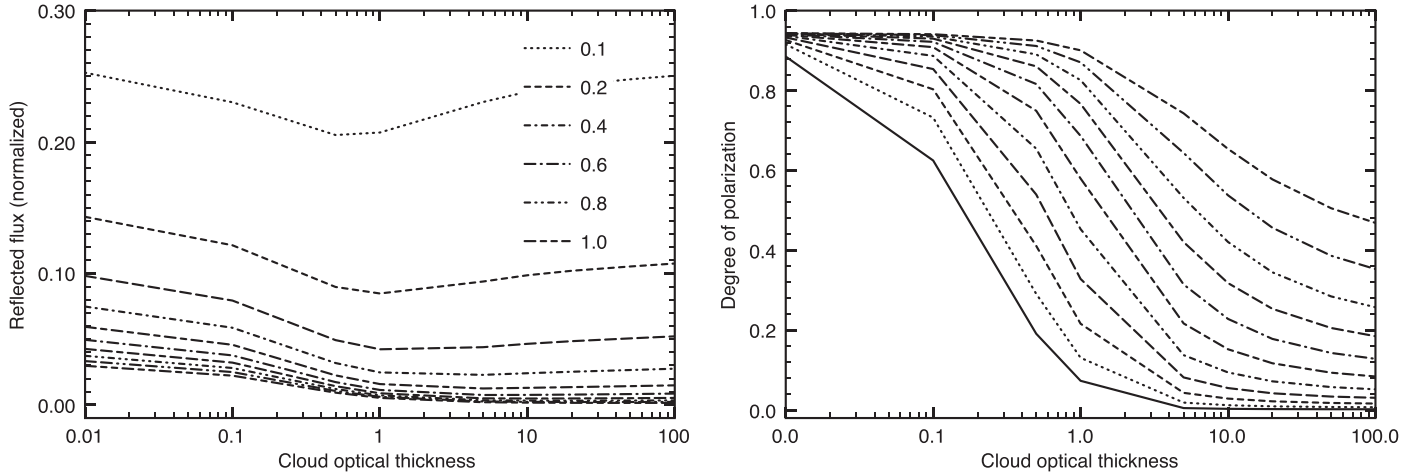

Figure 12. Similar to Figure 8 but as functions of $b_{\rm cloud}$. The cloud is 2 km thick and has its top at 6.0 km. The surface is black, and $\alpha = 90°$. The thick solid line pertains to $\eta = 0.0$.

parameters and mixing ratios are unknown, and the aim is to determine both.

Our computations show that there will be significant degeneracies if only the fluxes of reflected starlight are being used. Assuming that a planet is horizontally homogeneous and observed at a phase angle of 90°, a measured absorption band depth in flux F could be fitted with different O_2 mixing ratios η depending on the assumed cloud optical thickness (Figure 12) and cloud-top altitude (Figure 16). The surface albedo appears to be less of an influence (Figure 5). Here, we assume that only the relative fluxes are available, because absolute exoplanet fluxes can only be obtained when the planet radius and the distances to its star and observer are known (the flux of a small bright planet can equal that of a large dark planet).

Degeneracies are even more of a problem if the planet is assumed to be horizontally inhomogeneous. Our computations for inhomogeneous planets (with different mixing ratios, and patchy clouds with different coverage percentages, optical thicknesses, altitudes, and particle thermodynamic phases) show a wide range of band depths in the flux with significant overlap between the signals of various model planets. Including surface pressures different from those on Earth, clouds made of condensates other than water, atmospheric hazes, and/or other aerosols would increase the range of possible fits to the observations.

Measuring both the flux and the polarization of starlight that is reflected by a planet could help to reduce the degeneracies, because the band strength in polarization has a different sensitivity to the atmospheric parameters and surface albedo than the band depth in reflected flux. Indeed, assuming a horizontally homogeneous planet and a phase angle of 90°, measuring P would help to retrieve the cloud optical thickness; however, for optically thin clouds, the surface albedo would influence the signal, too. The sensitivity of the polarization depends on the mixing ratio: the larger the value of η, the larger the range of $b_{\rm cloud}$ the polarimetry is sensitive to. The polarization also holds information on the cloud-top altitude, although the mixing ratio should be known for an actual retrieval. Here, a combination with flux measurements could help. Retrieving cloud-top altitudes with an error of ± 2 km would require polarization measurements with a precision of 1%–2%.

Assuming horizontally inhomogeneous planets, the range of planet parameters that would fit a certain combination of flux and polarization measurements obviously increases. To diminish degeneracies, the observational precision should be increased, as subtle differences in flux and polarization could help to distinguish between different models. Measurements at several phase angles would also provide more information, as the degree of polarization in and outside the band depends strongly on the atmospheric parameters. Indeed, measurements at the rainbow phase angle (38°) would not only help to determine whether cloud particles are made of liquid water but also provide information on the cloud optical thickness. Hansen & Travis (1974) show a number of plots of the single-scattering polarization of particles with different compositions. An investigation into what would be the distinguishing rainbow phase angle for clouds made of such particles would help to plan observations but is outside the scope of this paper.

Another method of diminishing degeneracies would be to perform observations at a range of wavelengths. In particular, short wavelengths are more sensitive to scattering by gas and small particles than longer wavelengths and could thus provide more information about the amount of gas above the clouds (i.e., the cloud-top altitude) and possibly about the cloud patchiness (by reflecting more light from the cloud-free regions). Longer wavelengths are less scattered by the gas and small particles and thus give a better view of the clouds and surfaces. Because of the spectral information in both the flux and the polarization, not only in absorption bands but also in the continuum, it is essential to use narrowband observations rather than broadband observations.

A high temporal resolution would also help to identify the contributions of time-varying signals, such as the rotation of a planet with a horizontally inhomogeneous surface (a regular variation, not addressed in this paper) and/or weather patterns changing the CC (as on Earth, the CC could also depend on the surface properties, such as the presence of mountains). Our computations of the variability in the O_2 A-band depth and strength in flux and polarization due to different shapes and locations of cloud patches (Figure 20) illustrate which observational accuracy would be needed to resolve such variations, which depend on the CC and the mixing ratio.

In our models, the surface reflection is Lambertian, i.e., depolarizing. Various types of natural surfaces reflect linearly

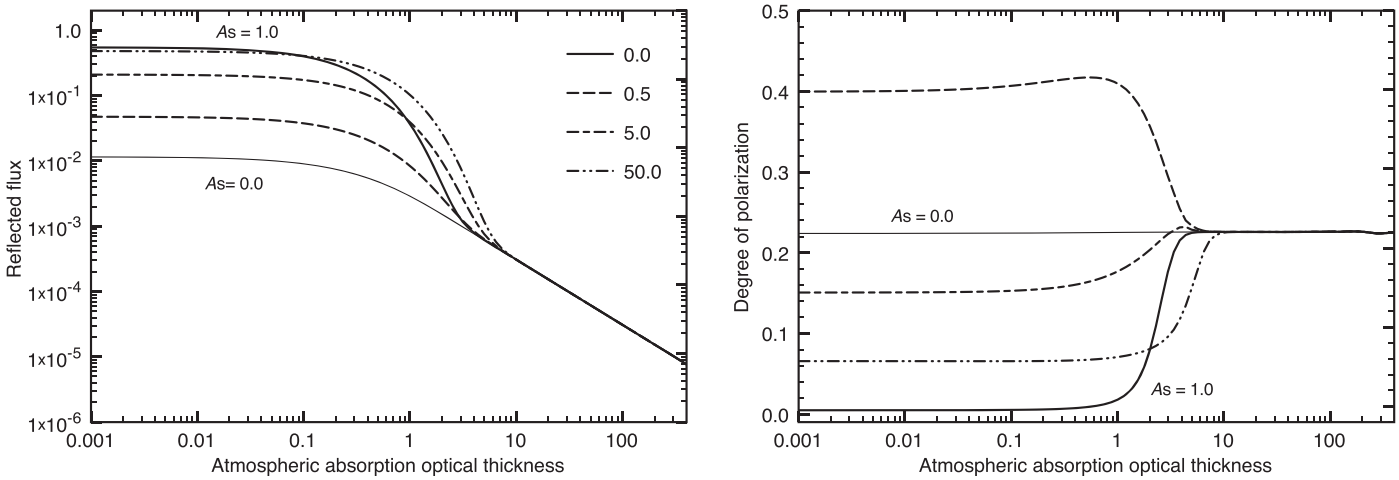

Figure 13. Similar to Figure 6, except for $\alpha = 38°$, the "rainbow" angle, and $b_{\rm cloud}$ equal to 0.5, 5.0, and 50.0. For comparison, the curves for cloud-free planets with black and with white surfaces have also been included.

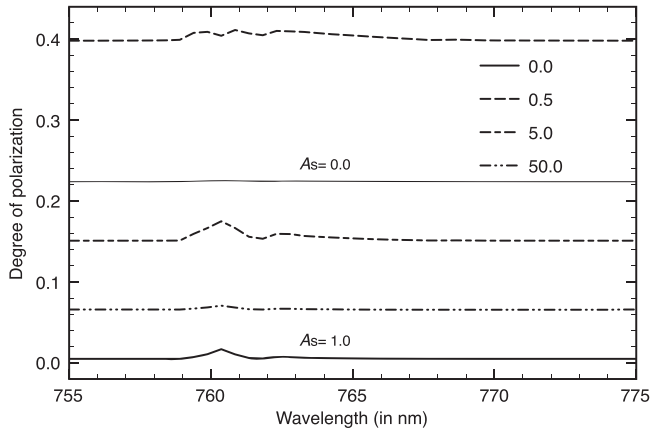

Figure 14. Similar to Figure 12 but for $\alpha = 38°$, the "rainbow" angle, and $b_{\rm cloud}$ equal to 0.5, 5.0, and 50.0. For comparison, the curves for black ($A_s = 0.0$) and white ($A_s = 1.0$) cloud-free exoplanets have also been included.

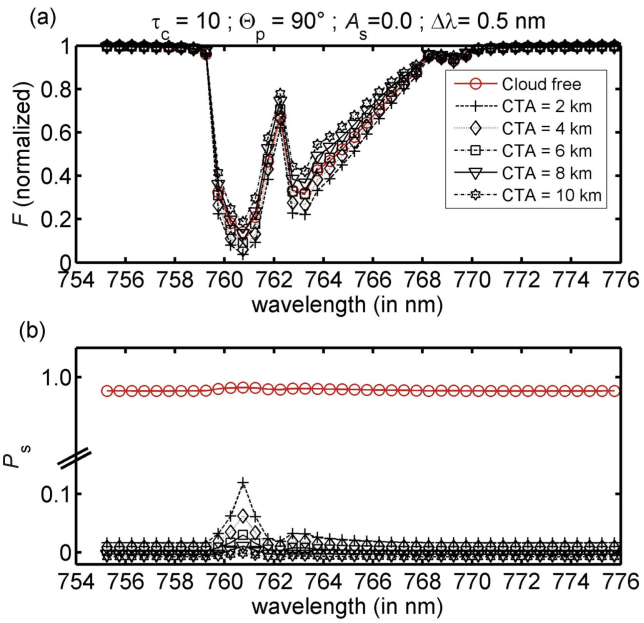

Figure 15. The F (top) and P_s (bottom) of starlight reflected by planets that are completely covered by a horizontally homogeneous cloud layer with $b_{\rm cloud} = 10$ that is 2 km thick. The cloud-top altitude ($z_{\rm top}$, or CTA in the plot) ranges from 2.0 to 10.0 km. The red curves are for cloud-free planets with $A_s = 0.0$ (cf. Figure 4). All flux curves have been normalized at 755 nm.

polarized light and sometimes also circularly polarized light (see, e.g., Patty et al. 2017 and references therein). Including such polarizing surfaces in our planet models would strongly increase the number of free parameters, and the influence of the polarizing surfaces could influence the continuum polarization for the regions on a planet that are cloud-free with at most a few percent provided the surface albedo is not too low (see Stam 2008 for results for a planet completely covered by a flat, Fresnel-reflecting ocean surface). For cloudy regions, no influence of the surface polarization is expected.

While our computations show that measuring the polarization would decrease the degeneracies in retrievals of mixing ratios of gases such as the biosignature O_2, they can also be used to optimize the design of instruments and/or telescopes. Indeed, many spectrometers are sensitive to the polarization of the observed light: the measured flux will depend on the polarization of the incoming light. Because the polarization will usually vary across a gaseous absorption band, any instrumental polarization sensitivity will change the shape and depth of the measured absorption bands. Unless carefully corrected for (which is difficult when the incoming polarization is not known, even when the instrumental polarization is accurately known), such changes will influence the retrieved gas mixing ratios. Typical absorption-band strengths in our polarization computations can be combined with (estimated) instrumental polarization sensitivities to estimate and possibly minimize the errors that could result.

These errors will strongly depend on the spectral resolution of the observations: the higher the spectral resolution, the higher the observable degree of polarization. This can be seen in Figure 3 and in the various figures that show F and P (or P_s) as functions of $b_{\rm abs}$, the atmospheric absorption optical thickness. Thus, the higher the spectral resolution, the more information can be obtained from observations, but the more care should be taken to account for instrumental polarization.

Current large ground-based telescopes with broadband photometric and polarimetric capabilities for exoplanet observations are SPHERE/VLT and GPI/Gemini North. Narrowband spectropolarimetry might become available in the near future on

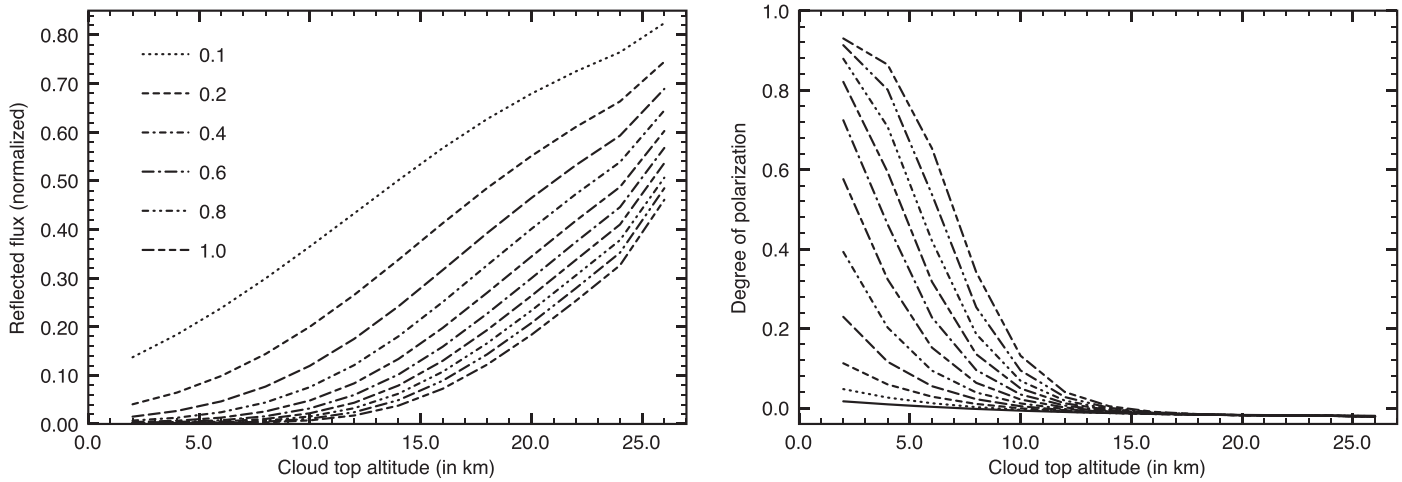

Figure 16. Similar to Figure 8 but as functions of z_{top} for $b_{cloud} = 10$, a geometrical thickness of 2 km, and $A_s = 0.0$. The O_2 mixing ratio η ranges from 0.0 (thick solid line, not shown in the flux as it equals 1.0) to 1.0 in steps of 0.1.

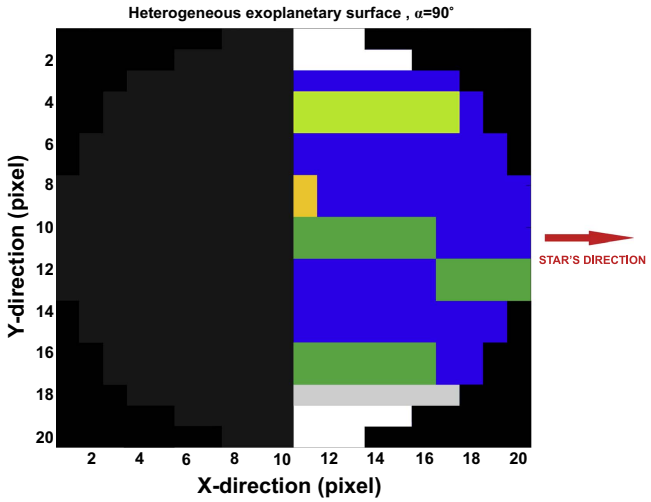

Figure 17. Our model planet with its heterogeneous surface and without clouds at $\alpha = 90°$. The colors of the pixels represent the following surface types: white = fresh snow regions (32 pixels @ $A_s = 0.9$); light gray = old and/or melted snow (15 pixels @ $A_s = 0.6$); light green = grassy lands (39 pixels @ $A_s = 0.25$); dark green = forests (50 pixels @ $A_s = 0.15$); yellow = sandy desert (30 pixels @ $A_s = 0.4$); and blue = ocean (150 pixels @ $A_s = 0.06$).

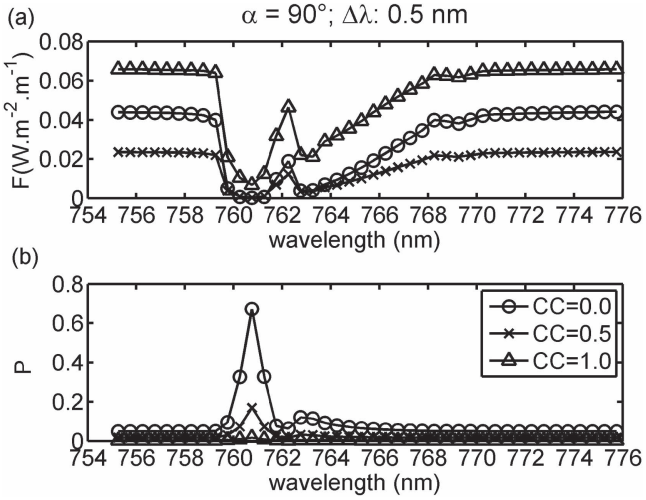

Figure 18. Similar to Figure 15 but for the heterogeneous model planet shown in Figure 17 ($\alpha = 90°$) without clouds (CC = 0.0), with half of the pixels covered by clouds (CC = 0.5), and with all pixels covered by clouds (CC = 1.0). The clouds have the following properties: 50% with $b_{cloud} = 50$, 16.7% with $b_{cloud} = 5$, 16.7% with $b_{cloud} = 10$ (all between 4 and 6 km altitude), and 16.5% with $b_{cloud} = 10$ (between 8 and 10 km).

EPICS/ELT and proposed space telescopes such as *WFIRST*, *LUVOIR*, or *HabEX* and provide us with the first spectra of the O_2 A-band to be used for the characterization of exoplanets (absorption line–resolving Doppler detections of exoplanetary O_2 might indeed succeed earlier and provide lower limits for the O_2 column density). Then, the difficulty will be to discard false-positive detections of O_2. For instance, dioxygen may not necessarily be a biosignature (Domagal-Goldman et al. 2014; Wordsworth & Pierrehumbert 2014; Harman et al. 2015; Schwieterman et al. 2016a, 2016b). Lifeless, terrestrial planets in the habitable zone of any type of star can develop oxygen-dominated atmospheres through photolysis of H_2O (e.g., Wordsworth & Pierrehumbert 2014) or CO_2 (e.g., Harman et al. 2015). However, O_2 due to CO_2 photolysis would not be detectable with current and planned space- and ground-based instruments on planets around F- and G-type stars. Planets around K stars and especially M stars may produce detectable abiotic O_2 because of the low-UV flux from their parent stars

Table 1
The Properties of the Six Model Cloud Types

Type	Phase	b_{cloud}	z_{bot} (km)	z_{top} (km)
1	liquid	0.2	4.0	6.0
2	liquid	5.0	4.0	6.0
3	liquid	10.0	4.0	6.0
4	liquid	50.0	4.0	6.0
5	liquid	10.0	6.0	8.0
6	solid	0.5	10.0	12.0

(Harman et al. 2015). Also, strong O_4 features that could be visible in transmitted spectra at 1.06 and 1.27 μm or in UV/VIS/NIR reflected light spectra by a next-generation direct-imaging telescope such as *LUVOIR*/HDST or *HabEx* could be a sign of an abiotic dioxygen-dominated atmosphere that suffered massive H escape (see Schwieterman et al. 2016a, 2016b). These considerations highlight the importance of wide spectral coverage for future exoplanet characterization missions

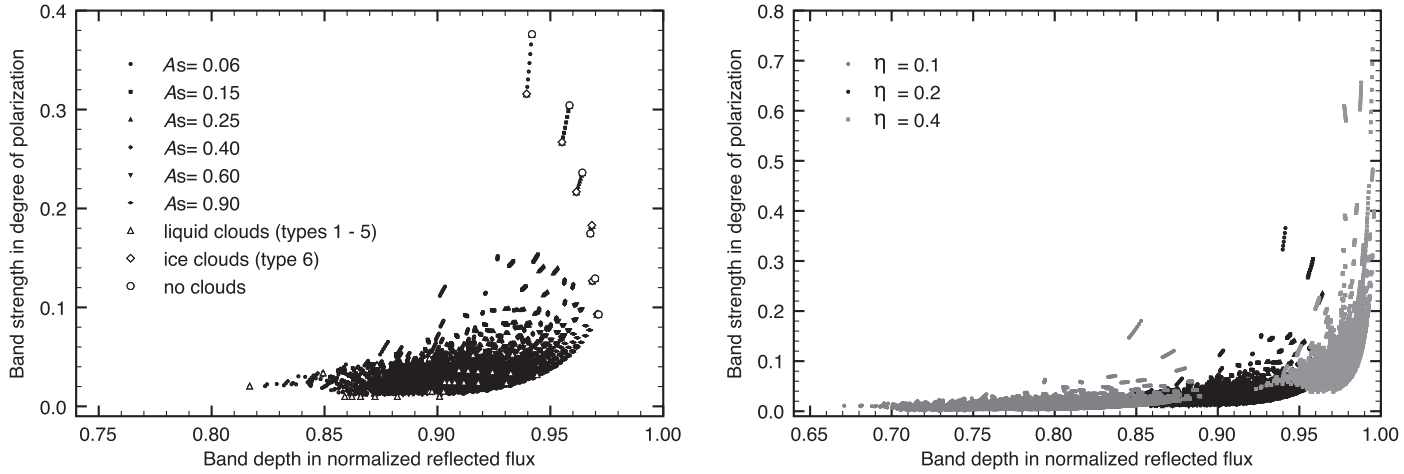

Figure 19. Similar to Figure 9 for $\eta = 0.2$ (left) and $\eta = 0.1$, 0.2, and 0.4 (right), $\alpha = 90°$. Each model planet has six possible values of A_s and cloud-free and/or cloudy pixels (of the six types in Table 1). Left: white symbols pertain to horizontally homogeneous planets. Dark symbols pertain to horizontally inhomogeneous planets. Right: data points for $\eta = 0.2$ partially overplotted by those for $\eta = 0.1$ (on the left side) and 0.4 (on the right side).

(Domagal-Goldman et al. 2014) and the combination of flux and polarization measurements in order to obtain as much information as possible from the limited numbers of photons.

5. Summary

We have computed the O_2 A-band feature in the flux and polarization spectra of starlight that is reflected by Earth-like exoplanets and investigated its dependence on planetary parameters. The O_2 A-band covers the wavelength region from about 755 to 775 nm, and it is the strongest absorption band of diatomic oxygen in the visible. Observations of the depth of this band in the reflected flux and the strength of the band in polarization could be used to derive the O_2 mixing ratio in the atmosphere of an exoplanet and with that provide insight into the possible level of photosynthetic processes on the planet.

In our model computations, we assumed that O_2 is well-mixed and that the clouds on a planet consist of water, like on Earth. We varied the O_2 mixing ratio η, the planetary surface albedo A_s, the cloud optical thickness b_{cloud}, the cloud-top altitude z_{top}, and the cloud fraction and spatial distribution over the planet. We computed both the flux F and the degree of linear polarization P (or P_s) of the starlight that is reflected by the model planet. Because of the difficulty of measuring absolute fluxes and polarizations of exoplanets (and without accurate knowledge of the distance to an exoplanet and its size, a measured reflected flux cannot be directly related to the albedo of the planet), we focus on the relative difference between F in the deepest part of the O_2 A-band (around 760.4 nm) and in the continuum outside the band (at 755 nm), with the latter normalized to 1. For P, which is independent of distances and planetary radii because it is a relative measure, we focus on the absolute difference between the polarization in the deepest part of the band and that in the continuum. We use a spectral bin width of 0.5 nm for the spectral computations, but values for narrower bins can be derived from computations of F and P as functions of the atmospheric absorption optical thickness.

While, as expected, F in the band is always smaller than F in the surrounding continuum, P in the band is higher than P in the continuum in most of our model computations, with strong variations in the band strength depending on the atmospheric and surface parameters. For absorption line–resolving observations, P will show even more variation with respect to its continuum value, especially in the deepest absorption lines and with vertical structure in the atmosphere, such as the presence of high-altitude ice clouds.

Our computations lead us to the following main conclusions:

1. For $\alpha = 90°$ and a given value of η, the band depth in (relative) F is very insensitive to the surface albedo A_s if it is larger than about 0.1 and the cloud optical thickness b_{cloud} if it is larger than about 0.5.
2. For $\alpha = 90°$, the band depth in (relative) F is sensitive to the cloud-top altitude z_{top}, although the sensitivity decreases for $\eta > 0.2$ and $z_{top} < 10$ km.
3. The band strength in P is very sensitive to A_s, except when $\eta > 0.7$ and for $30° < \alpha < 150°$. If $A_s \approx 0$, the band strength is smaller than 0.04 (for a spectral bin width of 0.5 nm).
4. The band strength in P is very sensitive to b_{cloud} as long as b_{cloud} is smaller than about 5 for $\eta = 0.2$. The band strength increases with η. If $\eta = 0.2$ and $b_{cloud} > 5$, the band strength is smaller than 0.04 (for 0.5 nm wide bins and $\alpha = 90°$).
5. The band strength in P decreases with z_{top}. For $\eta = 0.2$, the maximum band strength (for $z_{top} = 2$ km) is about 0.10 at $\alpha = 90°$.
6. For partly cloudy planets with or without horizontally inhomogeneous surface albedos below the atmosphere, the degeneracies are even larger. Variations in F and P measured over time could help to identify whether observed band depths and strengths are due to clouds or surface features.
7. Measuring both F and P appears essential to reducing the existing degeneracies due to the effects of the surface albedo, cloud optical thickness and altitude, and O_2 mixing ratios. Increasing the wavelength coverage (short and long wavelengths) and the phase angle range of the observations will also help to reduce degeneracies. In particular, phase angles close to the rainbow angle, i.e., 38°, would not only help with identifying the presence of liquid water particles, but the strength of the O_2 A-band in polarization at that phase angle can be used for cloud optical thickness retrieval.

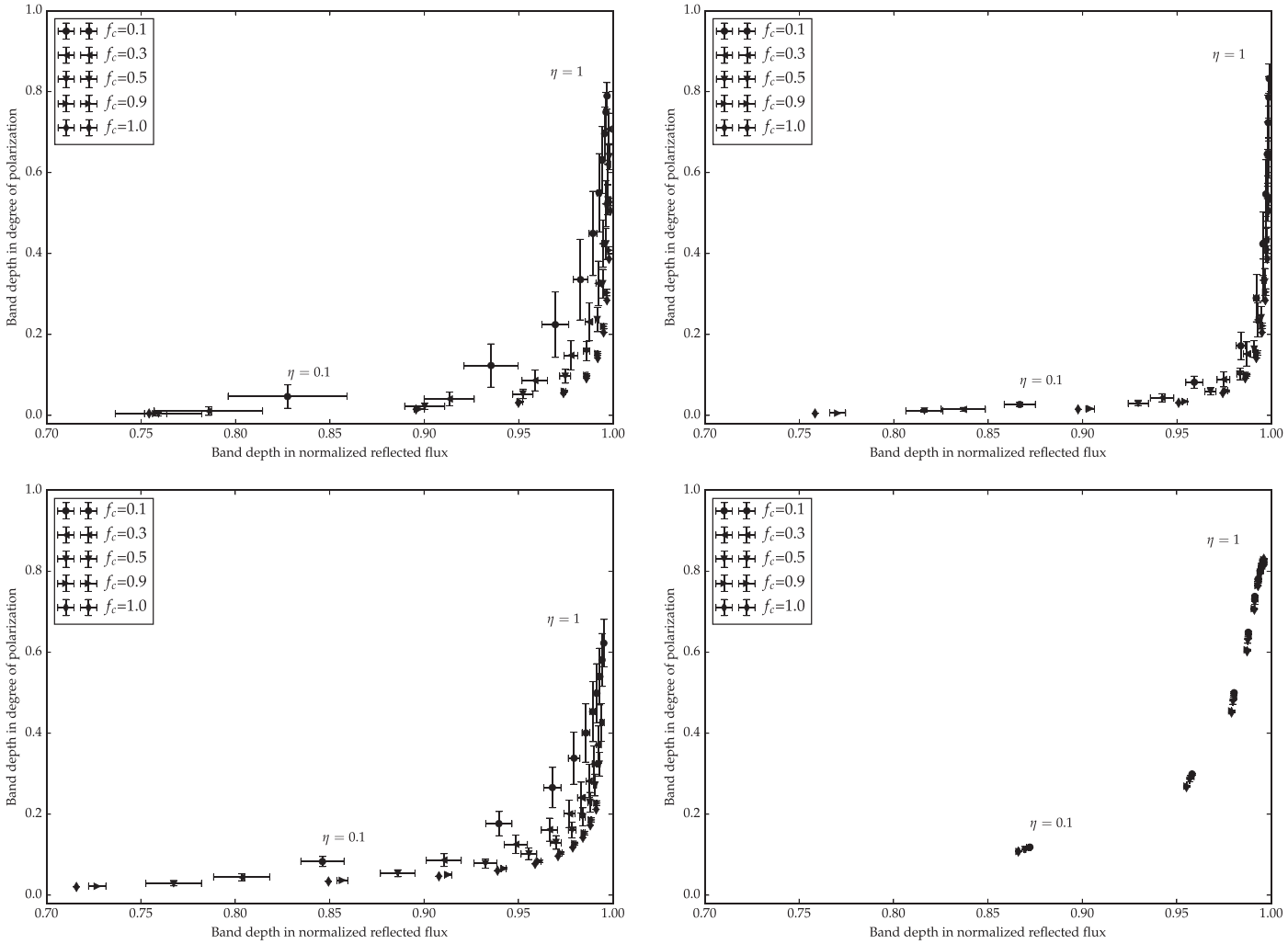

Figure 20. Similar to Figure 19 but for planets with patchy clouds and $\alpha = 90°$. Each planet has one value for A_s and one cloud type (see Table 1). Top left: $A_s = 0.15$, type 1. Top right: $A_s = 0.6$, type 1. Bottom left: $A_s = 0.15$, type 5. Bottom right: $A_s = 0.15$, type 6 (ice clouds). The error bars indicate the variance in the band depth in F and the band strength in P for the same value of CC (f_c in the plot) but for different distributions of the clouds. The mixing ratio η increases from 0.1 to 1.0 in steps of 0.1.

8. The band depth in F will increase and the band strength in P will become stronger (in vertically homogeneous atmospheres) with increasing spectral resolution, i.e., increasing spectral bin width. Absorption line–resolving observations of P would reveal a large variation in the behavior of P across the deepest absorption lines, particularly in the presence of high-altitude clouds or hazes.

The O_2 A-band is the strongest spectroscopic feature of dioxygen detection in reflected starlight. The retrieval of the O_2 mixing ratio will be difficult due to degeneracies that can occur for various combinations of cloud optical thickness, cloud altitude (similarly for hazes), and surface properties. Cloud composition, which we have not included in our study, would also play a role. To reduce the degeneracies, the flux and the polarization should be used together to provide information on the cloud optical thickness, particularly if measured at a range of phase angles and wavelengths.

We would like to thank the anonymous reviewer for the elaborate comments that allowed us to improve the quality of this paper. This work was initiated at the LOA, Lille 1 University, and completed during Thomas Fauchez's NASA Postdoctoral Program (NPP). This paper is not funded or sponsored by NASA.

References

Aben, I., Stam, D. M., & Helderman, F. 2001, GeoRL, 28, 519
Anglada-Escudé, G., Amado, P. J., Barnes, J., et al. 2016, Natur, 536, 437
Bailey, J. 2007, AsBio, 7, 320
Beuzit, J.-L., Feldt, M., Dohlen, K., et al. 2006, Msngr, 125, 29
Boesche, E., Stammes, P., Preusker, R., et al. 2008, ApOpt, 47, 3467
Bott, K., Bailey, J., Kedziora-Chudczer, L., et al. 2016, MNRAS, 459, L109
Crowe, S., Døssing, L., Beukes, N., et al. 2013, Natur, 501, 535
de Haan, J. F., Bosma, P. B., & Hovenier, J. W. 1987, A&A, 183, 371
de Rooij, W. A., & van der Stap, C. C. A. H. 1984, A&A, 131, 237
Deschamps, P. Y., Bréon, F. M., Leroy, M., et al. 1994, ITGRS, 32, 598
Desmons, M., Ferlay, N., Parol, F., Mcharek, L., & Vanbauce, C. 2013, AMTD, 6, 2533
Domagal-Goldman, S. D., Segura, A., Claire, M. W., Robinson, T. D., & Meadows, V. S. 2014, ApJ, 792, 90
Ferlay, F., Thieuleux, F., & Cornet, C. 2010, JApMC, 49, 2492
Fischer, J., Cordes, W., Schmitz-Peiffer, A., Renger, W., & Mörl, P. 1991, JApMe, 30, 1260
Fischer, J., & Grassl, H. 1991, JApMe, 30, 1245
Fougnie, B., Bracco, G., Lafrance, B., et al. 2007, ApOpt, 46, 5435
Froning, C., Osterman, S., Beasley, M., Green, J., & Beland, S. 2006, Proc. SPIE, 6269, 62691V

Fujii, Y., Turner, E. L., & Suto, Y. 2013, ApJ, 765, 76
Gisler, D., Schmid, H. M., Thalmann, C., et al. 2004, Proc. SPIE, 5492, 463
Goloub, P., Deuze, J. L., Herman, M., & Fouquart, Y. 1994, ITGRS, 32, 78
Goloub, P., Herman, M., Chepfer, H., et al. 2000, JGRD, 105, 14747
Gratton, R., Kasper, M., Vérinaud, C., Bonavita, M., & Schmid, H. M. 2011, in IAU Symp. 276, The Astrophysics of Planetary Systems: Formation, Structure, and Dynamical Evolution, ed. A. Sozzetti, M. G. Lattanzi, & A. P. Boss (Cambridge: Cambridge Univ. Press), 343
Groff, T. D., Kasdin, N. J., Limbach, M. A., et al. 2014, Proc. SPIE, 9147, 91471W
Hansen, J. E., & Hovenier, J. W. 1974, JAtS, 31, 1137
Hansen, J. E., & Travis, L. D. 1974, SSRv, 16, 527
Harman, C. E., Schwieterman, E. W., Schottelkotte, J. C., & Kasting, J. F. 2015, ApJ, 812, 137
Hovenier, J. W., & van der Mee, C. V. M. 1983, A&A, 128, 1
Hovenier, J. W., van der Mee, C. V. M., & Domke, H. 2004, Transfer of Polarized Light in Planetary Atmospheres; Basic Concepts and Practical Methods (Dordrecht: Kluwer)
Joos, F., & Schmid, H. M. 2007, A&A, 463, 1201
Karalidi, T., & Stam, D. M. 2012, A&A, 546, A56
Karalidi, T., Stam, D. M., & Hovenier, J. W. 2012, A&A, 548, A90
Kasting, J. F., Whitmire, D. P., & Reynolds, R. T. 1993, Icar, 101, 108
Kawata, Y. 1978, Icar, 33, 217
Keller, C. U. 2006, Proc. SPIE, 6269, 62690T
Keller, C. U., Schmid, H. M., Venema, L. B., et al. 2010, Proc. SPIE, 7735, 77356G
Kemp, J. C., Henson, G. D., Steiner, C. T., & Powell, E. R. 1987, Natur, 326, 270
Kemp, J. C., & Wolstencroft, R. D. 1971, Natur, 232, 165
Knibbe, W. J. J., de Haan, J. F., Hovenier, J. W., et al. 2000, JQSRT, 64, 173
Knibbe, W. J. J., de Haan, J. F., Hovenier, J. W., & Travis, L. D. 1998, JGR, 103, 8557
Koelemeijer, R. B. A., Stammes, P., Hovenier, J. W., & de Haan, J. F. 2001, JGRD, 106, 3475
Konopacky, Q. M., Barman, T. S., Macintosh, B. A., & Marois, C. 2013, Sci, 339, 1398
Lacis, A. A., & Oinas, V. 1991, JGR, 96, 9027
Lelli, L., Kokhanovsky, A. A., Rozanov, V. V., et al. 2012, AMT, 5, 1551
Lindstrot, R., Preusker, R., Ruhtz, T., et al. 2006, JApMC, 45, 1612
Macintosh, B. & Gemini Planet Imager instrument Team, Planet Imager Exoplanet Survey, G., Observatory, G 2014, American Astronomical Society Meeting Abstracts, #223, 229.02
Marshak, A., & Davis, A. B. 2005, 3D Radiative Transfer in Cloudy Atmospheres, Physics of Earth and Space Environments Series (Heidelberg: Springer)
McClatchey, R. A., Fenn, R. W., Selby, J. E. A., Volz, F. E., & Garing, J. S. 1972, Optical Properties of the Atmosphere, AFCRL-72.0497 (Bedford, MA: U.S.A.F. Cambridge Research Laboratories)
Osterman, S., Froning, C., Beasley, M., Green, J., & Beland, S. 2006, Proc. SPIE, 6269, 626930
Patty, C. H. L., Visser, L. J. J., Ariese, F., et al. 2017, JQSRT, 189, 303
Petigura, E. A., Howard, A. W., & Marcy, G. W. 2013, PNAS, 110, 19273
Preusker, R., Fischer, J., Albert, P., Bennartz, R., & Schüller, L. 2007, IJRS, 28, 1957
Rossi, L., & Stam, D. M. 2017, A&A, in press
Rothman, L. S., Jacquemart, D., Barbe, A., et al. 2005, JQSRT, 96, 139
Saiedy, F., Hilleary, D. T., & Morgan, W. A. 1965, ApOpt, 4, 495
Schmid, H. M., Gisler, D., Joos, F., et al. 2005, in ASP Conf. Ser. 343, Astronomical Polarimetry: Current Status and Future Directions, ed. A. Adamson et al. (San Francisco, CA: ASP), 89
Schwieterman, E. W., Meadows, V. S., Domagal-Goldman, S. D., et al. 2016a, ApJL, 819, L13
Schwieterman, E. W., Meadows, V. S., Domagal-Goldman, S. D., et al. 2016b, ApJL, 821, L34
Seager, S., Whitney, B. A., & Sasselov, D. D. 2000, ApJ, 540, 504
Sneep, M., de Haan, J. F., Stammes, P., et al. 2008, JGRD, 113, D15S23
Stam, D., de Haan, J., Hovenier, J., & Aben, I. 2000a, JGR, 14, 22379
Stam, D., de Haan, J., Hovenier, J., & Stammes, P. 2000b, JQSRT, 64, 131
Stam, D. M. 2008, A&A, 482, 989
Stam, D. M., De Haan, J. F., Hovenier, J. W., & Stammes, P. 1999, JGR, 104, 16843
Stam, D. M., de Rooij, W. A., Cornet, G., & Hovenier, J. W. 2006, A&A, 452, 669
Stam, D. M., & Hovenier, J. W. 2005, A&A, 444, 275
Stam, D. M., Hovenier, J. W., & Waters, L. B. F. M. 2004, A&A, 428, 663
Toubbé, B., Bailleul, Th., Deuzé, J. L., Goloub, Ph., Hagolle, O., & Herman, M. 1999, ITGRS, 37, 513
Vanbauce, C., Buriez, J. C., Parol, F., et al. 1998, GeoRL, 25, 3159
Vanbauce, C., Cadet, B., & Marchand, R. T. 2003, GeoRL, 30, 1212
Wang, P., Stammes, P., van der, A. R., Pinardi, G., & van Roozendael, M. 2008, ACP, 8, 6565
Wiktorowicz, S. J., Nofi, L. A., Jontof-Hutter, D., et al. 2015, ApJ, 813, 48
Wordsworth, R., & Pierrehumbert, R. 2014, ApJL, 785, L20
Yamamoto, G., & Wark, D. Q. 1961, JGR, 66, 3596
Young, A. T. 1981, JOSA, 71, 1142